



JGR Solid Earth



RESEARCH ARTICLE

10.1029/2019JB017997

Key Points:

- A 3-D model of Antarctica's lithosphere is derived from satellite gravity gradient data and self-consistent thermodynamic modeling
- Moho depth values show a root-mean-square misfit of less than 7 km with local seismic estimates at the points where data are available
- Mantle viscosity in West Antarctica is $\sim 10^{19}$ Pa·s, while the elastic lithosphere for GIA models is up to 150 km thick in East Antarctica

Supporting Information:

- Supporting Information S1
- Supporting Information S2
- Data Set S1

Correspondence to:

F. Pappa,
folker.pappa@ifg.uni-kiel.de

Citation:

Pappa, F., Ebbing, J., Ferraccioli, F., & van der Wal, W. (2019). Modeling satellite gravity gradient data to derive density, temperature, and viscosity structure of the antarctic lithosphere. *Journal of Geophysical Research: Solid Earth*, 124, 12,053–12,076. <https://doi.org/10.1029/2019JB017997>

Received 10 MAY 2019

Accepted 21 OCT 2019

Accepted article online 25 OCT 2019

Published online 16 NOV 2019

Modeling Satellite Gravity Gradient Data to Derive Density, Temperature, and Viscosity Structure of the Antarctic Lithosphere

F. Pappa¹ , J. Ebbing¹ , F. Ferraccioli², and W. van der Wal³

¹Department of Geosciences, Kiel University, Kiel, Germany, ²British Antarctic Survey, Cambridge, UK, ³Delft University of Technology, Delft, The Netherlands

Abstract In this study we combine seismological and petrological models with satellite gravity gradient data to obtain the thermal and compositional structure of the Antarctic lithosphere. Our results indicate that Antarctica is largely in isostatic equilibrium, although notable anomalies exist. A new Antarctic Moho depth map is derived that fits the satellite gravity gradient anomaly field and is in good agreement with independent seismic estimates. It exhibits detailed crustal thickness variations also in areas of East Antarctica that are poorly explored due to sparse seismic station coverage. The thickness of the lithosphere in our model is in general agreement with seismological estimates, confirming the marked contrast between West Antarctica (<100 km) and East Antarctica (up to 260 km). Finally, we assess the implications of the temperature distribution in our model for mantle viscosities and glacial isostatic adjustment. The upper mantle temperatures we model are lower than obtained from previous seismic velocity studies. This results in higher estimated viscosities underneath West Antarctica. When combined with present-day uplift rates from GPS, a bulk dry upper mantle rheology appears permissible.

Plain Language Summary The solid Earth structure of the Antarctic continent is still poorly explored due to the coverage of up to 4-km-thick ice sheets and its remote location. Robust knowledge of its characteristics is, however, essential to understand the Earth's response to ice mass changes (glacial isostatic adjustment). Of particular interest are the depth and geometry of the main subsurface boundaries, which are the interface between crustal and mantle rocks (Moho discontinuity) and the base of the rigid tectonic plate (lithosphere). Since both of them are accompanied by changes in rock density, we used gravimetric data from the Gravity Field and Steady-State Ocean Circulation Explorer satellite to build a 3-D model of Antarctica's deep structure. Rock composition according to temperature and pressure is taken into account. Rock composition according to temperature and pressure is taken into account and the model as a whole is internally consistent. As a result, we present a continental-scale Moho depth map that shows novel details. From the temperature distribution in our model, we derive present-day uplift rates of the solid Earth's surface, which are a key parameter in estimating the future ice sheet evolution.

1. Introduction

The structure of the Antarctic lithosphere is still less known than that of other continents. Agreement exists on a difference in lithospheric structure between West Antarctica (WANT) and East Antarctica (EANT) divided by the Transantarctic Mountains (TAM) and the Antarctic Peninsula (e.g., Torsvik & Cocks, 2013; Figure 1). WANT comprises several distinct Paleozoic to Mesozoic fore-arc and magmatic-arc terranes (Dalziel & Elliot, 1982) and the Ellsworth-Whitmore terrane with Grenville-age crust (Craddock et al., 2017). Multiple phases of rifting took place from Cretaceous to Cenozoic times in the West Antarctic Rift System (WARS; e.g., Fitzgerald, 2002; Jokat & Herter, 2016) and earlier rifting commencing in the Jurassic in the Weddell Sea region (e.g., Jordan et al., 2017). The tectonic history of EANT is characterized by several phases of accretionary or collisional events in the Precambrian (Boger, 2011). Thus, EANT is now widely recognized to comprise several lithospheric provinces of different origin and age, ranging from Archaean and Paleoproterozoic to Cambrian (Boger, 2011; Elliot et al., 2015; Ferraccioli et al., 2011; Harley et al., 2013; Torsvik & Cocks, 2013, and references therein).

Seismological methods are well suited for assessing the internal structure of the lithosphere. However, the remoteness and the harsh environment of the Antarctic continent make seismic experiments logistically

©2019. The Authors.

This is an open access article under the terms of the Creative Commons Attribution-NonCommercial-NoDerivs License, which permits use and distribution in any medium, provided the original work is properly cited, the use is non-commercial and no modifications or adaptations are made.

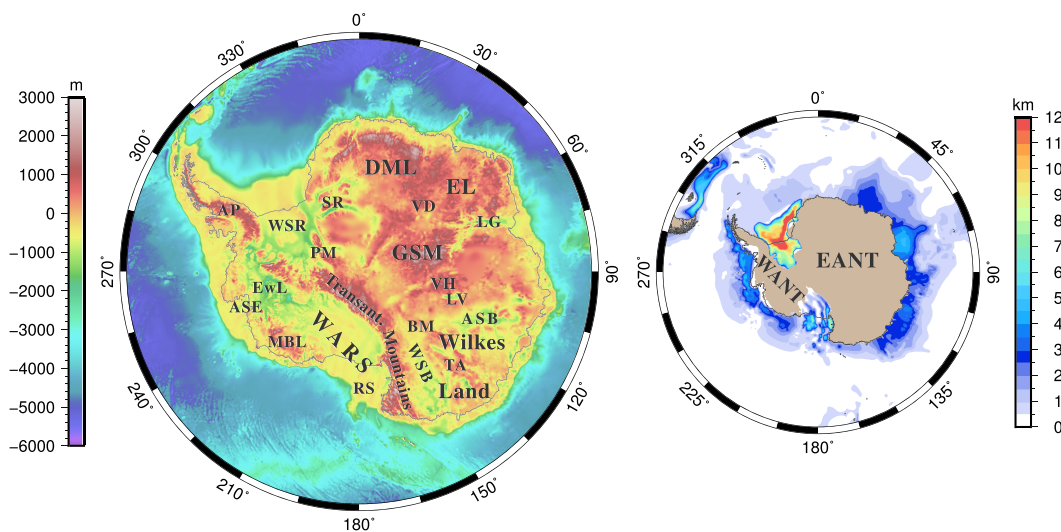


Figure 1. (left) Bedrock topography of Antarctica. AP = Antarctic Peninsula, ASB = Aurora Subglacial Basin, ASE = Amundsen Sea Embayment, BM = Beardmore Microcontinent, DML = Dronning Maud Land, EL = Enderby Land, EwL = Ellsworth Land, GSM = Gamburtsev Subglacial Mountains, LG = Lambert Graben, LV = Lake Vostok, PM = Pensacola Mountains, RS = Ross Sea, SR = Shackleton Range, TA = Terre Adélie, VD = Valkyrie Dome, VH = Vostok Highlands, WARS = West Antarctic Rift System, WSB = Wilkes Subglacial Basin, WSR = Weddell Sea Rift. (right) Sediment thickness data compilation used in this study. Sources are described in the main text. EANT = East Antarctica, WANT = West Antarctica.

and technically challenging. Recently, a number of seismological models for the Antarctic continent (e.g., An et al., 2015a; Hansen et al., 2014; Heessel et al., 2016; Ramirez et al., 2016) or with focus on WANT and TAM have been published (Graw & Hansen, 2017; Hansen et al., 2016; Lloyd et al., 2015; O'Donnell et al., 2017; Ramirez et al., 2017; Shen et al., 2018; White-Gaynor et al., 2019), which show the clear differences in crustal thickness between EANT and WANT and to a notable extent the heterogeneous nature of the upper mantle. However, density models derived from seismic observations generally lead to predicted gravity anomalies that differ greatly from observed values (Pappa et al., 2019) and therefore exhibit significant inconsistencies. Beyond that, gravity data or combinations of gravity and seismic data have been used to estimate the crustal thickness for the entire Antarctic continent (Baranov et al., 2018; Block et al., 2009; O'Donnell & Nyblade, 2014). Even though the main features are similar in these models, considerable disagreement exists in some regions, for example, in Wilkes Land or eastern Dronning Maud Land (DML) where seismic and gravity estimates of crustal thickness differ by over 10 km.

Alternatively, satellite gravity gradient data can be used in combination with seismological models to derive lithospheric models. The potential of satellite-based gravity gradients to establish regional models, which can be used as a background for local interpretations, has been demonstrated (Bouman et al., 2015; Holzrichter & Ebbing, 2016) and is especially useful for large, inaccessible areas such as the Antarctic continent (Ebbing et al., 2018). Since the gravity gradients possess different sensitivities for different depth ranges (Bouman et al., 2016), they are particularly suited to investigate the mass distribution within the lithosphere. Still, gravity gradient data alone are not sufficient to uniquely constrain density.

Few studies so far have tried to jointly investigate the crust and upper mantle (e.g., An et al., 2015a, 2015b; Haeger et al., 2019) of EANT, which is needed to better understand the fundamental structure of the lithosphere as a whole. Seismic velocities and rock densities depend on temperature and composition, which can be modeled by minimizing the Gibbs energy or described in simplified terms by other petrophysical parameters such as thermal expansion and compressibility. An et al. (2015b) estimated the temperature of the Antarctic lithosphere and upper mantle through conversion of seismic velocities (An et al., 2015a) by using a homogeneous noncratonic mantle composition. However, uncertainties caused by the potential presence of melt or fluid or linked to the choice of the anelasticity model adopted are higher than those arising from compositional variations within the lithosphere and remain difficult to fully resolve. The resulting temperature model was however an important step toward a better understanding of the state of Antarctica's lithosphere. Haeger et al. (2019) compiled existing seismological crustal thickness estimates and used satellite

gravity data to isolate the gravity signal from the lithospheric mantle. By also utilizing seismological velocity models, they iteratively derived a density, temperature, and compositional model of the Antarctic lithosphere. Their methodology, however, relies on the validity of the crustal model adopted, which is subject to high uncertainties.

An alternative approach is to incorporate the whole lithosphere and sublithospheric upper mantle in one model. In addition, integrated modeling of both geophysical and petrological properties of rocks in a self-consistent framework can help to reduce the uncertainties associated with modeling the observables separately (Fullea et al., 2012). This approach has proved valuable for investigation of the lithospheric structure in several studies (e.g., Fullea et al., 2015; Jones et al., 2014). The inferred temperature structure of a lithospheric model obtained by this process can also be used to also estimate sublithospheric upper mantle viscosity. Seismological models are typically used to derive a 3-D Earth viscosity structure. Nield et al. (2018) explored the effect of applying 3-D viscosity distribution instead of classical 1-D models on Antarctica and have shown that such models are crucial to obtain more accurate spatial patterns of glacial isostatic adjustment (GIA). However, deriving 3-D viscosity from seismological models introduces uncertainties from the seismological data and from the conversion methodology.

In this study we use satellite gravity gradient data, the principle of isostasy, and thermodynamic modeling of mantle petrology to derive a self-consistent 3-D lithospheric density and temperature model of the Antarctic continent. New crustal and lithospheric thickness estimates are obtained and compared with previous studies. The modeled upper mantle temperature field is then used to derive viscosity values and to compute present-day uplift rates due to GIA.

2. Data

The gravity gradients are the second derivative of the gravitational potential. They are generally more sensitive to shallower structures than the vertical gravity field, which makes them a useful tool to study the density structure of the lithosphere (Bouman et al., 2016). During the years 2009–2013 European Space Agency's satellite mission Gravity Field and Steady-State Ocean Circulation Explorer measured the gradients of the Earth's gravity field at an average altitude of 255 km at the beginning of the mission and 225 km at the end of the mission. For our study we use the gravity gradient grids at 225-km height (Figure 2) from Bouman et al. (2016). Commonly, gravity gradient data are expressed as tensor components in a North-West-Up frame, which is suitable for regions of intermediate latitudes, but leads to unintuitive maps in polar regions. By performing a tensor basis change, we adopt a local reference system for Antarctica. In this new IAU reference frame, the directions of derivation point to India (I; 90°E) and to the Atlantic Ocean (A; 0°E), that is, right and top in an Antarctic polar stereographic map, while the vertical axis (U; upward) remains unchanged. The components of the gravity vector T are rotated as a function of the longitude λ according to the following:

$$\begin{pmatrix} T_i \\ T_a \\ T_u \end{pmatrix} = \begin{pmatrix} \sin\lambda & -\cos\lambda & 0 \\ \cos\lambda & \sin\lambda & 0 \\ 0 & 0 & 1 \end{pmatrix} \begin{pmatrix} T_n \\ T_w \\ T_u \end{pmatrix}. \quad (1)$$

A complete derivation of equation (1) is presented in the supporting information.

To isolate the gravity gradient signal from the lithosphere, we first need to correct for the effect of topography, water, ice, and sediments. To achieve this, we use density values for water ($\rho_{\text{water}} = 1,028 \text{ kg/m}^3$), ice ($\rho_{\text{ice}} = 917 \text{ kg/m}^3$), and bedrock ($\rho_{\text{topo}} = 2,670 \text{ kg/m}^3$). The values adopted for ice thickness and topography were derived from the Bedmap2 Antarctic compilation (Fretwell et al., 2013). The Bedmap2 model describes the ice thickness and the bedrock topography (Figure 1) of Antarctica up to latitude 60°S and is mainly based on airborne radar surveys. Even though some areas are not well covered and exhibit large uncertainties up to >1,000 m, it is the most accurate ice thickness model currently available for Antarctica. (The effect of the uncertainty in the Bedmap2 model on the gravity gradients at satellite altitude is shown in supporting information Figure S4.) The gravity gradient effect of the individual units for the reduction is computed by discretization in tesseroids of ~11-km edge length south of 60°S and 0.5° edge length north of 60°S. A tesseroid is a segment of a sphere, delimited by upper and lower

meridians and parallels plus by its top and bottom radii (as distance from the Earth's center). In addition to assessing the gravity effect, the topographic data are used as a constraint for isostasy in our modeling. Regarding this issue, the model does not explicitly include an ice layer, which is why we use the rock-equivalent topography, in which the ice layer is converted into a mass-equivalent layer of rock density (e.g., Hirt et al., 2012), to evaluate the isostatic state.

Several low-lying sectors of the Antarctic bedrock host major sedimentary basins, which can cause significant gravity anomalies, depending on their thickness and the density and porosity of the infill. To assess the effect of sedimentary thickness on the gravity gradient signal over Antarctica, we compiled available models and data (Figure 1). Few studies exist for onshore areas of the continent (e.g., Aitken et al., 2014; Frederick et al., 2016), where relatively high sediment densities are to be expected due to additional compaction from the thick ice sheet. Because the density is close to that of the surrounding crystalline rock, we do not include sedimentary basins in onshore areas to avoid inducing regional inconsistencies, which would emerge from omission of relatively unexplored basins. In offshore areas, we use National Geophysical Data Center's global 5-arc min grid (Whittaker et al., 2013), which provides ocean sediment thickness estimates up to 70°S. We complement these with the more detailed model from Wobbe et al. (2014), which also covers the Ross Sea, the Amundsen Sea, and the Bellingshausen Sea. A sedimentary thickness map for the Weddell Sea is available based on the magnetic data presented by Golynsky et al. (2001) and suggests up to 15-km-thick sediments there. Although it is difficult to derive the crystalline basement depth reliably from magnetic anomalies, we include this data set due to the lack of alternative areal sediment thickness information for the Weddell Sea. A potential overestimation may lead to erroneously low densities in the upper crust that would have to be compensated by modeled higher densities at greater depths. Further analyses of newly compiled Antarctic magnetic anomaly data (Golynsky et al., 2018) may help enhance our current knowledge of sedimentary basin thickness within the Weddell Sea and other interior parts of the continent.

For the sediment density, we use a simple exponential compaction model (e.g., Chappell & Kusznir, 2008). Thus, the sediment density ρ is related to the depth z in km from the sediment top as follows:

$$\rho = \rho_g + (\rho_w - \rho_g) \Phi e^{-\lambda z}, \quad (2)$$

where ρ_g is the grain density (set to $\rho_g = 2,670 \text{ kg/m}^3$), ρ_w is the water density (set to $\rho_w = 1,028 \text{ kg/m}^3$), Φ is the porosity of the uppermost sediment, and λ is the exponential decay constant. We use data from Slater and Christie (1980), who provide $\Phi = 0.55$ and $\lambda = 0.4 \text{ km}^{-1}$ as representative values for mixed or unknown marine sediments. Global far-field gravitational effects are accounted for water and rock topography, usingETOPO1 topography (Amante & Eakins, 2009), which seamlessly extends the Bedmap2 model, with the same values for ρ_{water} and ρ_{topo} as indicated above. Offshore sediments up to 30°S are also taken from the National Geophysical Data Center grid (Whittaker et al., 2013).

After subtraction of the effect of ice, water, bedrock topography, and sediment density anomaly from the observed gravity gradient data, a signal is obtained that should mainly reflect subsurface density variations in the crystalline crust and in the mantle (Figure 2). However, the remaining signal may still contain effects of an imperfect topographic reduction model or effects of deep mantle density heterogeneities. Moreover, the lithosphere may be in a state of isostatic disequilibrium due to ice mass changes in the past (O'Donnell et al., 2017). This GIA-induced displacement of the solid Earth can cause a gravity signal that should be considered if it is significant. The effect on the gravity gradients at satellite altitude (225 km), however, accounts at maximum for ~25 mE (Figure S6), corresponding to less than 1% of the total signal, and is thus small enough to be neglected.

3. Modeling Methods

3.1. Lithospheric Modeling

A combined modeling framework of multiple geophysical quantities of the lithosphere and the sublithospheric upper mantle is provided by the forward modeling software LitMod3D (LITHospheric MODelling in a 3-D geometry; Fullea et al., 2009). It solves the equations for heat flow, thermodynamic properties of

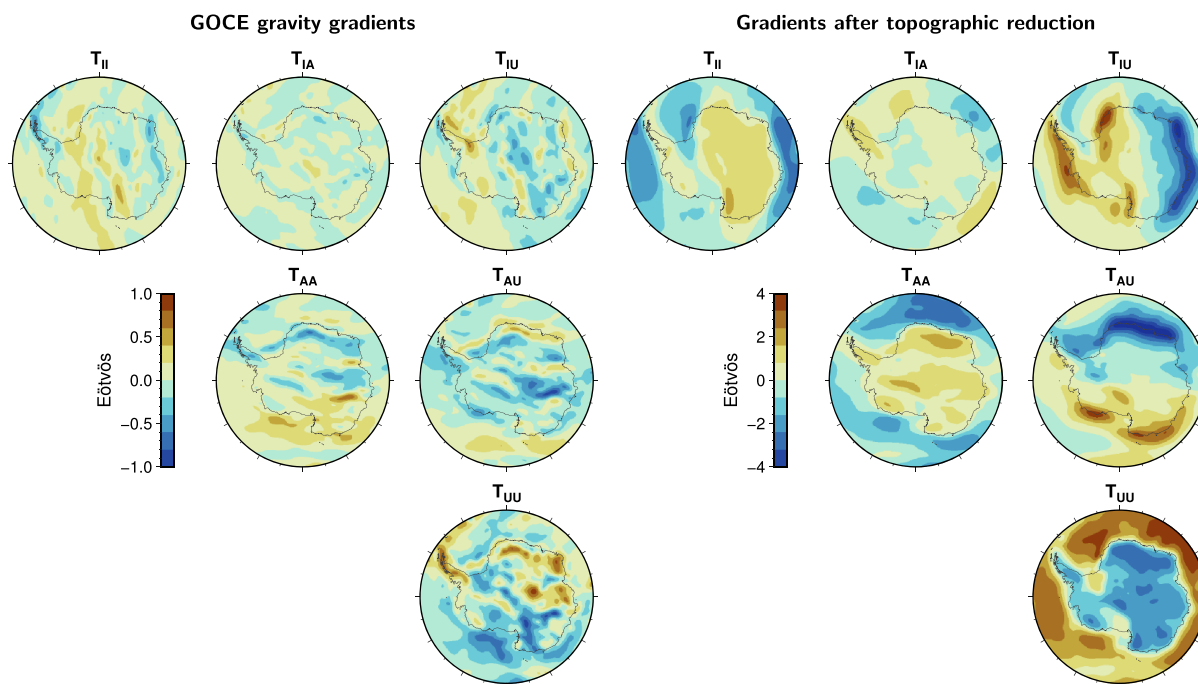


Figure 2. (left) GOCE derived gravity gradients at 225-km altitude (Bouman et al., 2016). (right) The same data after reduction for effects of water, ice, rock topography, and sediments. Note the change of signal amplitude. GOCE = Gravity Field and Steady-State Ocean Circulation Explorer.

rocks, gravitation, and isostasy simultaneously in a finite differences method. Output quantities are density, temperature and pressure fields, surface heat flow, seismic body wave velocities, geoid, gravity anomalies, and isostatic elevation (topography). The underlying material properties are functions of temperature, pressure, and composition. LitMod3D uses a combined petrological (compositional), rheological (isostatic) and thermal (1315 °C isotherm) definition of the lithosphere-asthenosphere boundary (LAB).

Generally, the LAB is defined as the boundary between the rheologically strong lithospheric mantle and the rheologically weak asthenospheric upper mantle, where partial melting occurs (Artemieva, 2009, and references therein). Laboratory experiments indicate a sharp change in rheology and elastic properties of olivine-rich rocks at temperatures between 85% and 100% of the solidus temperature (Sato et al., 1989; Sato & Sacks, 1989) and thus connect the rheological definition with a thermal boundary in the range of 1250–1350 °C. Different geophysical methods can be used to detect the LAB, depending on the according definition, which with their pitfalls are discussed in detail in Artemieva (2009) and Eaton et al. (2009). For example, from seismic methods the LAB can be defined as a change in anisotropy or as the boundary between a (*S* wave) high-velocity lid and low velocities in the asthenosphere. For GIA modeling, the transition from purely elastic to viscoelastic behavior on glacial time scales determines the bottom of the lithosphere (Nield et al., 2018, and references therein), which does not necessarily coincide with any of the previously mentioned LAB definitions (Artemieva, 2009). This transition is governed by viscosity, which is the crucial parameter for GIA studies (Paulson et al., 2005; Wu, 2005) and can be derived through conversion of temperatures by using power law rheology (Nield et al., 2018).

In the following, we provide a short overview of the methodology of LitMod3D (for more details, the reader is referred to Fullea et al., 2009). The specific values of the modeling parameters such as densities will be presented in the subsequent section.

The model space is discretized into a regular Cartesian grid, and cells are assigned to specific layers. Thus, a geometry and geophysical parameters need to be predefined. In the simplest case, a model may consist of a crust, a lithospheric mantle, and a sublithospheric mantle layer. Each cell inherits the layer-specific geophysical parameters: bulk density, compressibility and thermal expansion coefficient, thermal conductivity, and radiogenic heat production. For computing heat transfer, LitMod3D assumes a conduction-dominated

lithosphere, where the thermal structure is calculated with the common steady-state (time-invariant) heat equation. While the thermal conductivity of the crust is constant, the thermal conductivity in the mantle follows the temperature- and pressure-dependent model of Hofmeister (1999). The upper and lower thermal boundary conditions of the conduction-dominated region are defined by a constant surface temperature and a constant temperature at the LAB, respectively. Below the LAB, a buffer layer is modeled to represent both conduction and convection in a rheologically active layer between the lithosphere and the sublithospheric mantle down to a depth where the temperature reaches 1400 °C. Further down, convective heat transfer is simulated by an adiabatic gradient between the temperature at the bottom of the model at 400 km and 1400 °C isotherm. The bottom temperature is set to 1500 °C, which is consistent with high-pressure and high-temperature experiments (Fullea et al., 2009, and references therein).

The in situ density in crustal layers follows the formula for thermal expansion and compression:

$$\rho(T, P) = \rho_0 - \rho_0 \alpha (T - T_0) + \rho_0 \beta (P - P_0), \quad (3)$$

in which ρ_0 is the bulk density, α the thermal expansion coefficient, and β the compressibility. In subcrustal layers, densities are calculated with the thermodynamic modeling software Perple_X (Connolly, 2005) for given geochemical mantle compositions in the CaO, FeO, MgO, Al₂O₃, and SiO₂ scheme under mantle pressure and temperature conditions. Since more than 98% of the mantle is made up of these oxides (e.g., McDonough & Sun, 1995), they are considered to be a good basis for modeling mantle phase equilibria (Afonso et al., 2008). By minimization of the Gibbs free energy, the stable mineral phases and the consequent bulk rock densities can be computed according to several thermodynamic databases, which are based on laboratory experiments. We use the formalism and database for peridotites from Stixrude and Lithgow-Bertelloni (2005).

For Airy-type local isostasy, the pressure corresponding to the overlying density column is calculated for every node at the bottom of the model space (compensation level). The resulting elevation due to buoyancy forces is obtained from comparison with a reference density column at a mid-oceanic ridge and can be used as a quantity to fit the model to the actual topography in the study area. The reference at the mid-oceanic ridge is chosen because average elevations, petrogenetic processes, and lithospheric structures are better known there than in other tectonic settings (Afonso et al., 2008). Dynamic loads associated with sublithospheric mantle flows are neglected. Likewise, the error for Airy-type isostasy emerging from the planar approximation of the Earth is negligibly small due to the relatively thin lithosphere compared to the Earth's radius (Hemingway & Matsuyama, 2017). To take into account the rigidity of the lithosphere, regional (flexural) isostasy is modeled on the basis of the local isostasy, the pressure at the compensation level, and the assumed elastic thickness (T_e) of the lithosphere with the software TISC (Garcia-Castellanos, 2002). For our modeling we choose a value of $T_e = 30$ km.

Although LitMod3D is capable of calculating gravity gradients, this is still done in a Cartesian coordinate system. To account for the large extension of Antarctica, a spherical geometry should be used to avoid biased results. We thus use the software Tesseroids (Uieda et al., 2011), which can compute the gravitational potential, the gravity, and the gravity gradient effect caused by tesseroids with certain densities. We transform the lithospheric density model from LitMod3D into a spherical tesseroid model. An equiangular discretization in polar regions, however, would lead to very small tesseroids near the pole and bigger tesseroids at higher latitudes. A discretization into metrically equal sized tesseroids is a better choice, considering both numerical precision and computational effort. To avoid edge effects, we extend the model up to latitude 30°S. From the Cartesian LitMod3D model, an inner high-resolution (~25-km edge length) model is created up to a latitude of 60°S. Beyond that, coarser tesseroids (0.5°) are built. If a tesseroid of the extension model lies outside the original LitMod3D model space, the density of the particular depth layer is extrapolated and assigned to the tesseroid. A piece-wise linear reference model (Figure 3) with density increasing with pressure in the crust (above 30 km) and the mantle (below 30 km), is subtracted from the modeled in situ (absolute) densities.

3.2. GIA Modeling

For the GIA response a model is used that is based on the finite element software ABAQUS™, which computes the deformation for certain surface loads. Iterative calculations are required to account for changing

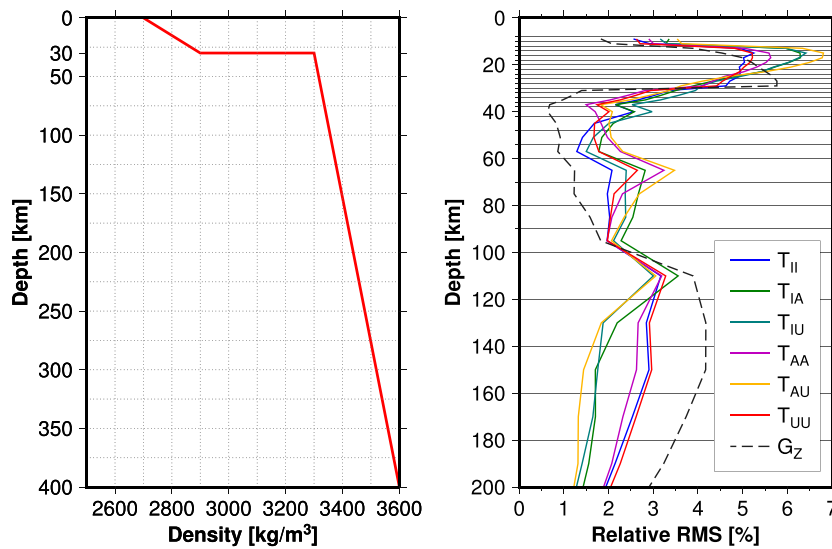


Figure 3. (left) A step-wise linear reference density model is used to compute relative density anomalies and gravity gradient anomalies. (right) Relative depth sensitivity of vertical gravity G_Z and gravity gradients for the final model. Horizontal lines mark the thickness of the contributing depth interval. The gradients generally show high sensitivity at depths above 100 km. T_{IA} , T_{IU} , and T_{AU} obtain their largest contribution from the uppermost 25 km, reflecting the density variation across continent-ocean transitions. Compare Figure S11 for absolute root-mean-square (RMS) values.

noneustatic sea level and the gravitational potential, which result in a new load to be applied at boundaries (Wu, 2004). Density and rigidity are derived from volume averaging of Preliminary Reference Earth Model (PREM) (Dziewonski & Anderson, 1981). Three-dimensional density structure, mainly the difference between EANT and WANT, could influence results, but our method requires 1-D density. Earlier work that included variation of 1-D density profile suggests limited effects for spatial wavelengths above 700 km (Vermeersen & Sabadini, 1997). Three-dimensional variation in elastic parameters was found to introduce small effects on elastic response (Mitrovica et al., 2011) and is therefore not included. The finite element model uses a stress-strain-rate relation for composite rheology (van der Wal et al., 2010; van der Wal et al., 2013). The composite rheology is based on experimental flow laws for olivine of Hirth and Kohlstedt (2003), which are assumed to be valid for the upper 400 km where olivine is the dominant mineral. The lithosphere our GIA model is implicitly defined in the model as that part of the top of the Earth model that does not deform viscously in the time scale of glacial loading. Barnhoorn et al. (2011) derived that this cutoff viscosity of 10^{25} Pa·s, above which no viscous deformation takes place, would be detectable in GIA measurements.

Viscosity, η_{eff} , is computed as in van der Wal et al. (2015):

$$\eta_{eff} = \frac{1}{3B_{diff} + 3B_{disl}q^{n-1}} \quad (4)$$

with q as the von Mises stress, n as the stress exponent (set to 3.5), and B_{diff} and B_{disl} contain all rheological parameters from the creep law for diffusion and dislocation creep in olivine:

$$B = Ad^{-p}fH_2O^r e^{\alpha\varphi} e^{-\frac{E+PV}{RT}}, \quad (5)$$

in which A and α are constants, d is the grain size, fH_2O is water content, Φ is melt fraction, E is activation energy, P is pressure, V is activation volume, R is the gas constant, T is absolute temperature, p is the grain size exponent, and r is the water fugacity exponent, respectively. Except for grain size and water content, all values are taken from Hirth and Kohlstedt (2003, Table 1). Pressure is calculated as a function of depth and density as obtained from PREM; temperature is taken from the LitMod3D model interpolated on the $2^\circ \times 2^\circ$ grid of the finite element model using triangular based linear interpolation. The viscosity in equation (4) is stress dependent. That means that there is a weak dependence on the ice load, for which we use the W12 model (Whitehouse et al., 2012). O'Donnell et al. (2017) suggested GIA and sublithospheric tectonic stress

levels to be of the same order of magnitude, which means that the viscosity will also depend on the tectonic stress. We neglect the influence of background stress here, as accurate predictions requires the stress tensor from both processes to be known.

B_{diff} below 400 km is set to $1.1 \cdot 10^{-21} \text{ Pa}^{-1} \cdot \text{s}^{-1}$ (corresponding to a viscosity of $1.1 \cdot 10^{21} \text{ Pa} \cdot \text{s}$). Outside the LitMod3D space, the top 100 km is taken to be elastic close to the value obtained in global GIA model (Peltier, 2004). Below 100 km, a diffusion creep parameter is used that corresponds to a viscosity of $1 \cdot 10^{21} \text{ Pa} \cdot \text{s}$. To reduce edge effects, creep parameters across the boundary are smoothed by applying a moving average to the log base 10 values of the creep parameters in a range of 8° before and after the boundary.

Applying an olivine flow law to derive viscosity introduces many uncertainties. Here we consider water content and grain size as unknown parameters as they have a large effect on viscosity for values that are still within their uncertainty bounds. In principle, those quantities can be measured in xenoliths but they do not provide a single, typical grain size. Furthermore, it is not certain how well the grain size and water content of the surfaced rocks represent conditions at depth. Also, the scarcity of xenolith samples in Antarctica makes it difficult to use them as constraints for flow law parameters. Hence, we opt to use values for grain size and water content that result in acceptable viscosities as determined from their good fit to GIA observations in other regions (van der Wal et al., 2013). Uncertainty in other parameters is absorbed by the grain size and water content. We do not include the influence of partial melt as O'Donnell et al. (2017). Viscosity and present-day uplift rates are shown for our temperature model for dry rheology and 4-mm grain size (4d, the preferred model in van der Wal et al., 2015), while uplift rates from wet rheology (1,000-ppm water content) and varying grain sizes are also investigated. It is important to note the Antarctic-wide loading model that we use here does not include recent ice load changes, which are expected to dominate present-day uplift rates in some regions in Antarctica (e.g., Barletta et al., 2018; Nield et al., 2014).

4. Model Setup

To cover the whole Antarctic continent at a reasonable resolution, our model extends over $6,620 \text{ km} \times 6,620 \text{ km}$ with a lateral resolution of 50 km. Vertically, the model extends down to 400 km, and a smaller vertical discretization of 2 km is chosen for reasons of numerical precision in computing the heat transfer. An initial structure is needed to start the model, ideally solely based on seismic estimates to be independent from our gravity gradient modeling. We use the continental-scale crustal thickness model AN1-CRUST (An et al., 2015a) since it is not a compilation of different regional studies but derived from Rayleigh wave analyses, constrained by Moho depth estimates from studies using receiver function techniques. The crustal thickness values from AN1-CRUST are the distance from the solid surface to the Moho, so we subtracted the surface elevation data from Bedmap2 in order to obtain the Moho depth with respect to the WGS84 reference ellipsoid and refer to the product as AN1-Moho (Figure 4). A continent-wide estimate of the lithospheric thickness is provided by the model AN1-LAB (Figure 4) from An et al. (2015b). The authors inverted temperatures from mantle S wave velocities (An et al., 2015a) and defined the LAB as the shallowest position with a temperature crossing the 1330°C adiabat. As described in section 1, the inferred mantle temperatures of this model may be overestimated due to omission of potential presence of melt or water. However, we regard the AN1-LAB to be a good initial geometry for our modeling. The An et al. (2015b) temperature model will be used for comparison with our final lithospheric model.

Given the lack of knowledge about characteristics of the lithosphere for large parts of Antarctica, particularly the interior of EANT, we take general (global) geophysical and petrophysical properties for crustal and lithospheric mantle rock parameters, but we distinguish between different domains vertically and horizontally (Table 1). Both the crust and the lithospheric mantle in our models are divided into an oceanic and a continental part. Since the actual ocean-continent transition at Antarctica's margins is still ill constrained in some regions, we use bathymetric data from the Bedmap2 and theETOPO1 data sets to determine the continental shelf line (taken at 2,000-m water depth) and take this as a proxy for the boundary of the continental lithosphere. We divide the continental crust into three layers of equal thickness (upper, middle, and lower crust). In this way we are able to model the thermal field more realistically by introducing differentiated radiogenic heat production rates and thermal conductivity, and we can vary the vertical density

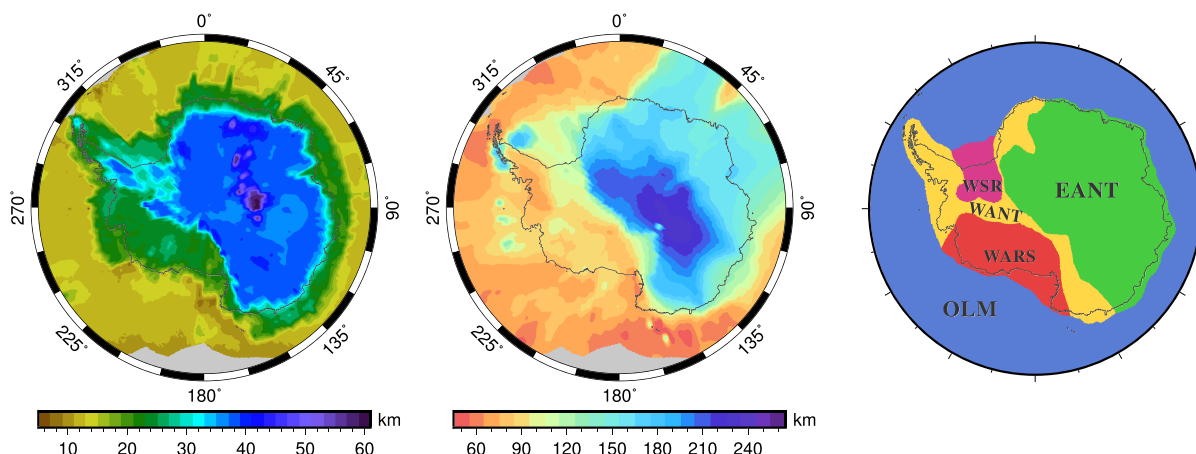


Figure 4. Initial model geometry for Moho and LAB depth is taken from seismological estimates: AN1-Moho (left, An et al., 2015a), AN1-LAB (center, An et al., 2015b). The right map shows the subdivision of lithospheric mantle domains in the model based on previous studies on tectonic provinces of Antarctica. EANT = East Antarctica, OLM = Oceanic lithospheric mantle, WANT = West Antarctica, WARS = West Antarctic Rift System, WSR = Weddell Sea Rift; LAB = lithosphere–asthenosphere boundary.

distribution within the crust. We use the same values as An et al. (2015b) for the thermal parameters, such that our modeled heat flow can be compared to their estimates.

To define different lithospheric mantle domains, we followed overviews of the Antarctic tectonic provinces (e.g., Boger, 2011; Goodge & Fanning, 2016; Harley et al., 2013), which rely on petrological evidence. The subcontinental lithospheric mantle is divided into three major domains (Figure 4): EANT, WANT, and the two major rift systems: the WARS (Bingham et al., 2012) and the Weddell Sea Rift (Jordan et al., 2017). We use representative lithospheric mantle compositions of Phanerozoic age for WANT and Proterozoic age for EANT (Table 2). Peridotitic xenolith samples from the WARS indicate a very heterogeneous lithospheric mantle structure (e.g., Armienti & Perinelli, 2010; Storti et al., 2008; Wörner, 1999), partly characterized by metasomatic processes and reenrichment of depleted lithospheric mantle. Since our model is not supposed to account for such localized variations, we assume a primitive upper mantle composition (McDonough & Sun, 1995) for the rift systems. Parts of EANT are assumed older than Proterozoic (Elliot et al., 2015; Goodge & Fanning, 2016; Ménot et al., 2007). For these regions, we implement an Archaean lithospheric mantle composition in some of our models as explained later on. Yet since such a depleted composition leads to very low densities, we implement it only in the upper lithosphere, accounting also for potential refertilization by postdepletion metasomatism of the lower lithosphere (e.g., Beyer et al., 2006). In oceanic areas, the lithospheric mantle is modeled in two layers in order to represent the vertically varying chemical composition and density due to differences in the degree of melt depletion in the mantle material generated at the mid-ocean ridge (e.g., Afonso et al., 2007; Ji & Zhao, 1994). The lower layer of oceanic

Table 1
Petrological Parameters of Crustal Layers in the Final Model (Model 3)

Type	Heat production ($\mu\text{W}/\text{m}^3$)	Thermal conductivity ($\text{W}/(\text{mK})$)	Density (kg/m^3)	Thermal expansion (K^{-1})	Compressibility (GPa^{-1})
Sediments	0.5	1.85	2,300	1E-5	8E-10
Upper crust	1.0	2.35	2,670	1E-6	1E-10
Middle crust	0.4	2.25	2,670	1E-6	1E-10
Lower crust	0.4	2.0	2,800	1E-6	8E-11
Oceanic crust	0.1	3.0	2,950	0	0
Mantle layers	0.01	5.3	—	—	—

Note. The in situ density is computed as a function of thermal expansion and compression according to temperature and pressure conditions. The thermal conductivity within the mantle follows the equations from Hofmeister (1999). The denoted value represents thermal conductivity at standard temperature-pressure conditions (Fullea et al., 2009).

Table 2*Oxide Composition of Lithospheric Mantle Peridotites Used for the Modeling*

wt %	PUM ^a	Lherzolite ^b	Harzburgite ^c	Phanerozoic ^d	Proterozoic ^d	Archaean ^d
SiO ₂	45.45	45.08	43.48	44.99	45.19	46.08
MgO	38.18	42.70	46.26	40.24	43.16	45.88
Al ₂ O ₃	4.55	2.42	1.96	3.54	1.93	1.00
FeO	8.18	8.44	7.80	8.09	8.00	6.45
CaO	3.64	1.36	0.50	3.13	1.72	0.59
Mg#	89.27	90.02	91.36	89.87	90.58	92.69

Note. PUM = primitive upper mantle.^aMcDonough and Sun (1995). ^bMaaløe and Aoki (1977). ^cIrfune and Ringwood (1987). ^dFullea et al. (2009) and references therein.

lithospheric mantle makes up two thirds of the total lithospheric mantle thickness in our model and has a lherzolitic composition, while the upper layer (one third of the total thickness) is modeled as harzburgite.

5. Results and Discussion

An iterative process was adopted to fit the model outputs to the observational data sets, that is, the rock-equivalent topography and the gravity gradient anomaly field at satellite height. The simple starting model with the initial geometry based on seismological data turns out to be far from isostatic equilibrium and does not satisfy the gravity gradient observations. Therefore, we proceed from this simple starting model and refine it in three subsequent stages:

1. Model 1 keeps the petrological parameters and the lithospheric domains from the initial model. The depths of the Moho and LAB interfaces are iteratively changed in the model in order to fit the isostatic elevation to the observed rock-equivalent topography. For this purpose, in each iteration step the current elevation misfit between the model and the data is multiplied with a factor that relates the topographic load with the mass deficit or surplus, respectively, at the interface through simple Airy isostasy. A detailed description of the method is given in the supporting information (Text S1). The resulting model is not a unique solution because, theoretically, isostatic equilibrium can be achieved with a variety of pairs of factors for adjusting the Moho and the LAB depth. However, the internal modeling processes, which determine the density in each cell of the model, significantly narrow the set of solutions (e.g., Afonso et al., 2013). After achieving isostatic equilibrium in Model 1 in this way, high residuals of more than ± 1 E are still present in the gravity gradients in some areas (Figure S8), which is ~25% of the amplitude of the topography-reduced input data. As an explanation, this misfit could be related to an improper vertical density structure of the model's lithosphere. For isostasy, only the mass integral is relevant. The gravity gradient components, on the other hand, have different depth sensitivities.
2. In Model 2, we account for these gravity gradient residuals by refining crustal and lithospheric domains while still maintaining isostatic equilibrium. Additional blocks of Archaean mantle lithosphere are introduced and the density parameters of the overlying crust are changed in regions with large misfits (Figure S9). The vertical density distribution is modified in such a way that the upper lithospheric mantle is less dense (depleted Archaean composition), whereas the crustal density is increased. Simultaneously, the Moho boundary and the LAB are shifted again to achieve isostatic equilibrium with the result that the crust is thinned and the lithospheric mantle is thickened, and thus, crustal material is replaced by denser mantle peridotite. Moreover, by shifting the isotherm that defines the LAB to greater depths, the middle to lower lithospheric mantle becomes denser due to temperature decrease. As a result, the gravity gradient response of Model 2 is improved by a few tenths of eötvös in the respective regions. It was, however, not possible to fit both the isostatic equilibrium and the gravity gradient field simultaneously.
3. Model 3 builds upon Model 2, but the previous constraint of isostatic balance of the Antarctic continent is discarded. Instead, the depth of the Moho discontinuity and LAB is adjusted based on the gravity gradient residual with accordingly different factors but in principle the same procedure as described for the isostatic fitting. As a result, the residual of the gravity gradients is generally less than ± 0.2 E (Figure 5), thus less than 5% of the topography-reduced signal. In turn, the root-mean-square (RMS) misfit between

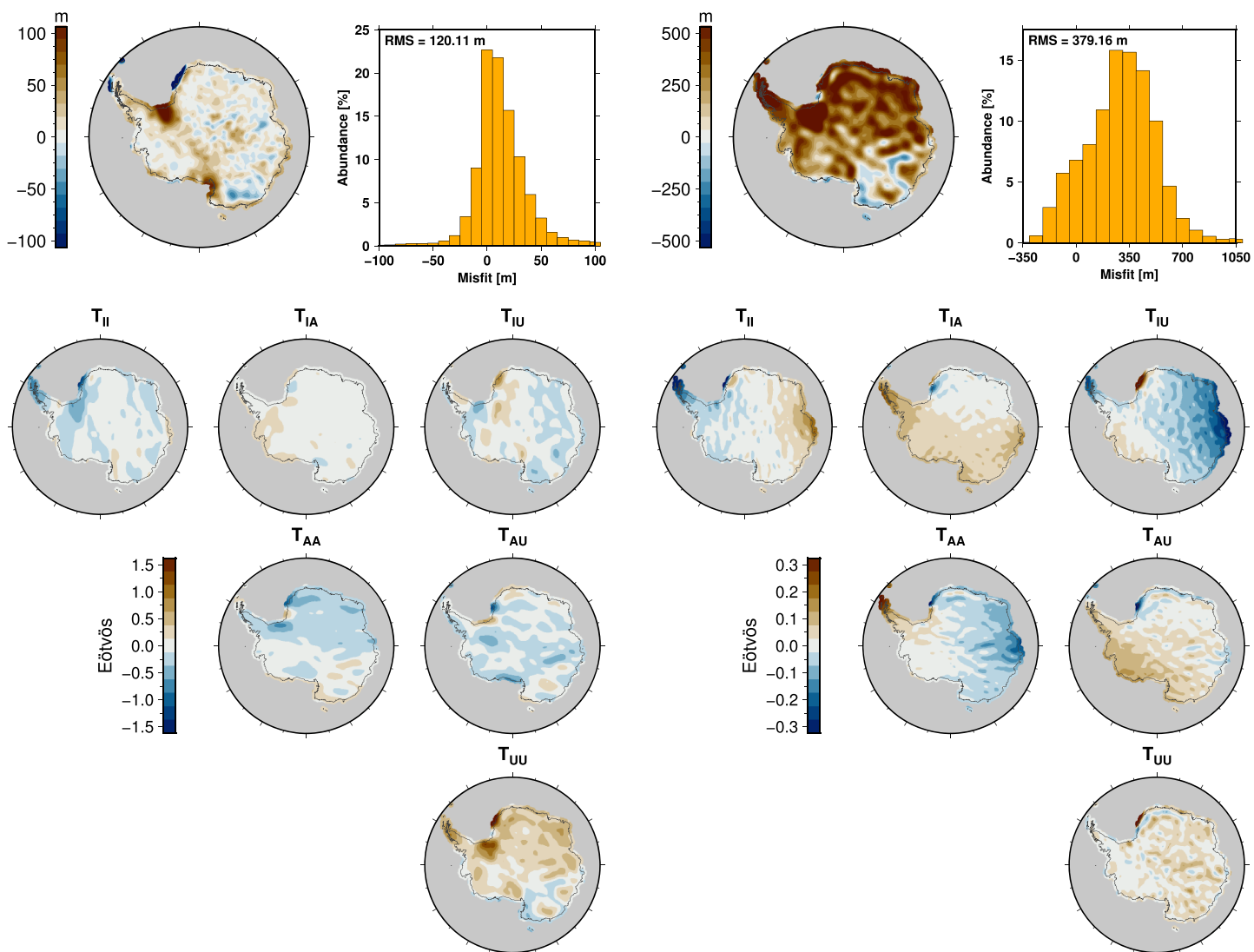


Figure 5. Residual analysis Model 2 (left) and Model 3 (right). (top) Topography misfit map and histogram. (bottom) Misfit of gravity gradient signal. Note the different value ranges. The gravity gradient misfit is reduced significantly from Model 2 (± 1 E) to Model 3 (± 0.2 E), though at the expense of the fit of perfectly isostatically compensated topography. The difference in elevation of ~ 250 m, mostly emerging in East Antarctica, may point to an imperfect topographic gravity correction model, flexural compensation, or dynamic forces that support the topography.

modeled and observed topography is 389 m (Figure 5). The patterns of the residual topography correlate with the gravity gradient (T_{UU}) residuals in Model 2 since the mass change in the subsurface is reflected by an increased or decreased isostatic elevation, respectively. These adjustments have implications for the isostatic state of different parts of Antarctica. In the following subsections, we will discuss and interpret the particular characteristics of the models in terms of crustal and lithospheric thickness, density, and temperature.

5.1. Topography Misfit in Gravity Gradient Fitted Model

By establishing isostatic equilibrium, a first-order fit of the gravity and gravity gradient field can usually be achieved (e.g., Braatenberg et al., 1997). This approach indeed reduces the gradient misfit of Model 1 significantly compared to the initial model, which was not in isostatic balance. It is, however, uncertain to what extent the Antarctic continent actually is in isostatic equilibrium. If sublithospheric forces generate a non-isostatic component in the present topography, fitting the observed gravity gradient field is a better option than fitting the isostatic elevation, because the gradients are most affected by near-surface density

variations. Furthermore, given the high accuracy and the homogeneous covering of the gravity gradient data over Antarctica, we consider Model 3 as our preferred model for a representation of the continent's lithospheric density structure. However, because the condition of perfect isostatic equilibrium is released, it shows a mismatch with the actual (rock-equivalent) topography (Figure 5). While no clear contrast is apparent between WANT and EANT in the residual map, Wilkes Land shows a distinctly different (negative) signature from the rest of EANT. Yet some parts of Wilkes Land still show positive residuals, specifically where the Archaean to Mesoproterozoic Terre Adélie Craton is located (e.g., Lamarque et al., 2015; Ménot et al., 2007) and where the inferred Paleoproterozoic Beardmore Microcontinent (Boger, 2011; Borg et al., 1990) is thought to underlie parts of the Wilkes Subglacial Basin (e.g., Ferraccioli et al., 2009; Ferraccioli & Bozzo, 2003) region (Figure 1).

In summary, these topography residuals are not explained by the gravity gradient signal. Their large-scale variations may be induced by sublithospheric forces like mantle upwellings or downwellings, which provide dynamic support of the topography. Short-wavelength residuals could originate from imperfect topographic or ice correction models onshore or sediment models in offshore areas. It is also possible that they represent topographic masses that are not in local isostatic balance but compensated regionally due to lithospheric flexure (e.g., Paxman et al., 2019). However, the RMS misfit of ~380 m is still small compared to the corresponding crustal thickness variation that would be needed to compensate such a topographic load. Assuming a rock density for the topography of $2,670 \text{ kg/m}^3$ and a density contrast at the Moho of 400 kg/m^3 , a 2.5-km-thicker crust would compensate 380 m of topography. This is below the uncertainty of most seismic-inferred Moho depth estimates even in well-studied areas.

5.2. Density Structure

A main advantage of using the full gravity gradient tensor in lithospheric modeling is the potentially different depth sensitivity of the individual components. The theoretical sensitivity kernels for the gravity gradients show a large response for near-surface mass anomalies (Martinec, 2014). However, the actual contribution of each depth interval depends on the location of the sources in the respective study area. An appropriate way to quantify this contribution is to compute the relative RMS of the signal of density variations with respect to the reference model (Bouman et al., 2016). For every single component of the gravity gradient tensor—and the vertical gravity G_z , respectively—the contribution of a particular depth interval is given in percentage of the total RMS integral over the depth. Figure 3 (right) shows the relative RMS signal contribution from different depth ranges computed for our lithospheric Model 3. (For absolute values see Figure S11.) For the vertical gravity and all gradient components, the strongest signal originates from a depth range of 10 to 25 km, which reflects the density variations at the continent-ocean boundaries. Horizontal and mixed components are more sensitive to signals at this depth than the vertical gradient T_{UU} and the vertical gravity G_z . From 25- to 40-km depth, the contrast between EANT and WANT affects the gradients more than the vertical gravity, resulting in a smoother decrease of the RMS with depth. In particular, the horizontal component T_{IA} , which is commonly considered to be most sensitive to very shallow structures, is still remarkably strong at this depth. Clearly, this reflects the sharp transition at roughly $45^\circ\text{W}/135^\circ\text{E}$ between WANT and EANT. Furthermore, a noticeable divergence of the T_{AU} and T_{AA} components is present at ~60-km depth. This means that a marked density variation exists with an orientation perpendicular to the 0° meridian (pointing toward the Atlantic), which is the Pacific-Antarctic Ridge north of the Ross Sea region. The density of the upper mantle is decreased to $3,200 \text{ kg/m}^3$ here in order to fit the bathymetry, whereas other regions in the model show $3,300 \text{ kg/m}^3$ and more in ~60-km depth. In summary, for almost every single layer above 100-km depth, the relative RMS contribution is higher in the gravity gradients than in the vertical gravity, even below the Moho.

The modeled densities of the upper mantle in our Model 3 are shown in Figure 6. At depths of 50 to 80 km the topography of the LAB is dominating the patterns in WANT with rather low densities in the coastal areas. In EANT the deep crustal root of the Gamburtsev Subglacial Mountains (GSM) stands out in the 50-km depth slice, whereas at 80-km lower density is present in areas where our model features Archaean lithospheric mantle composition. Down to 150 km, the mantle density is lower beneath WANT due to the higher temperature compared to cratonic EANT (Figure 6e). However, this relation is reversed below 150 km. At this depth, relatively low density values are present beneath EANT (Figure 6f), and the deep lithospheric mantle of EANT is notably less dense than the sublithospheric mantle of WANT, particularly at

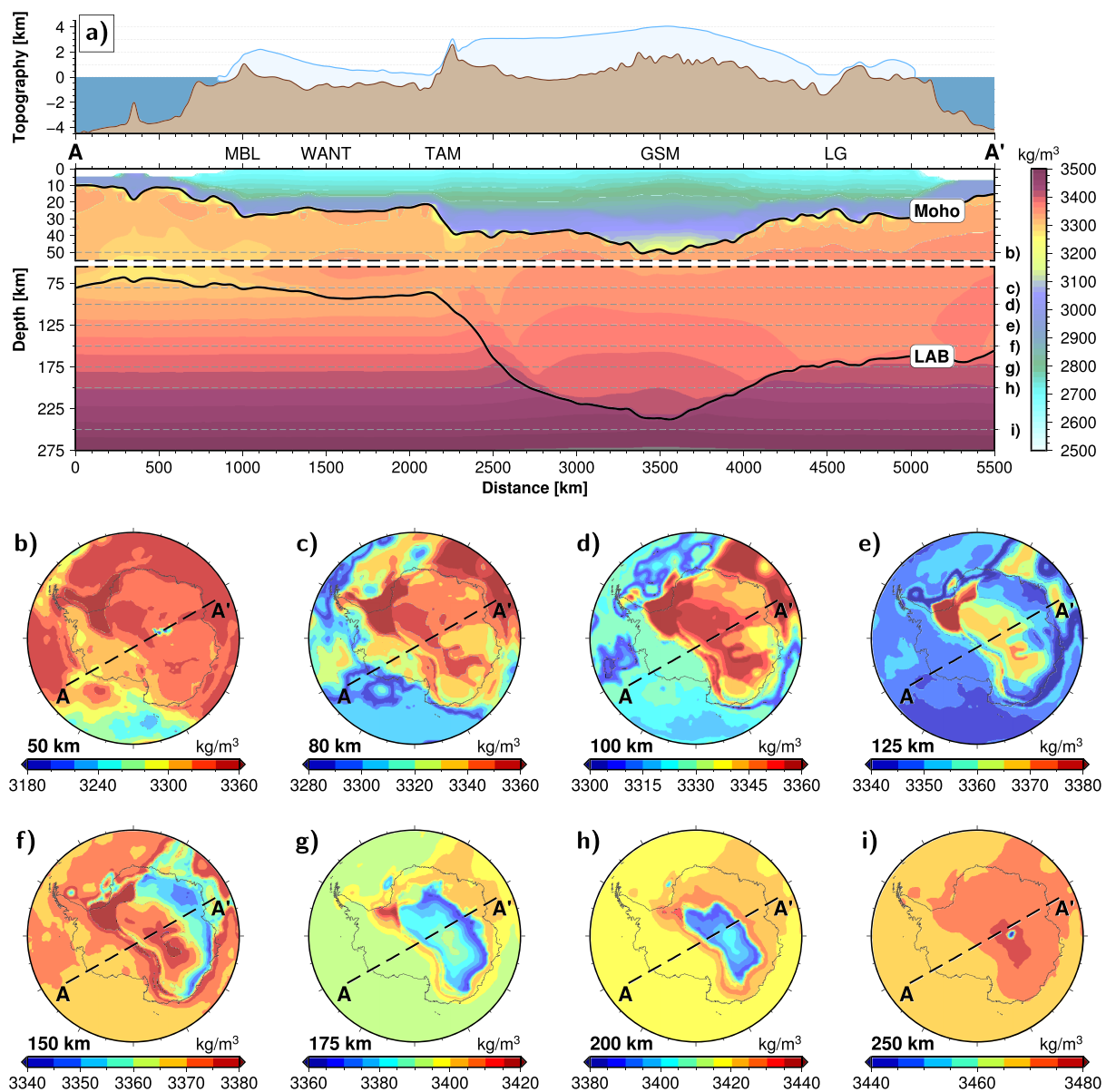


Figure 6. (a) Cross section through ice, topography, crust, and mantle of our Model 3. The profile is shown in the slices below. High crustal densities are present beneath the GSM. The mantle cross section illustrates the different density contrasts at the lithosphere-asthenosphere boundary beneath WANT and EANT, respectively. MBL = Marie Byrd Land, WANT = West Antarctica, TAM = Transantarctic Mountains, GSM = Gamburtsev Subglacial Mountains, LG = Lambert Graben. Dashed horizontal lines indicate depths of mantle density slices: (b) 50, (c) 80, (d) 100, (e) 125, (f) 125, (g) 175, (h) 200, and (i) 250 km.

its edges where it is hotter than in the interior. A cross section through the model is shown in Figure 6a that spans from the West Antarctic coast of Marie Byrd Land (MBL) across the WARS, the TAM, the GSM, and the Lambert Graben to the Indian Ocean coast, thus covering key elements of Antarctica's lithospheric structure over a distance of 5,500 km. It reveals another interesting feature: At the depth of the shallow LAB beneath WANT almost no density contrast is present between lithosphere and asthenosphere since the lithospheric mantle is relatively fertile, hot, and at low pressure. On the other hand, the density contrast at the deep lithospheric base of EANT adds up to several tens of kilograms per cubic meter and thus contributes to the lithosphere's buoyancy and the gravitational field anomalies. However, we note that our model does not include potential density variations in the asthenosphere due to temperature anomalies, as one would expect in case of a (WARS) mantle plume (e.g., Seroussi et al., 2017).

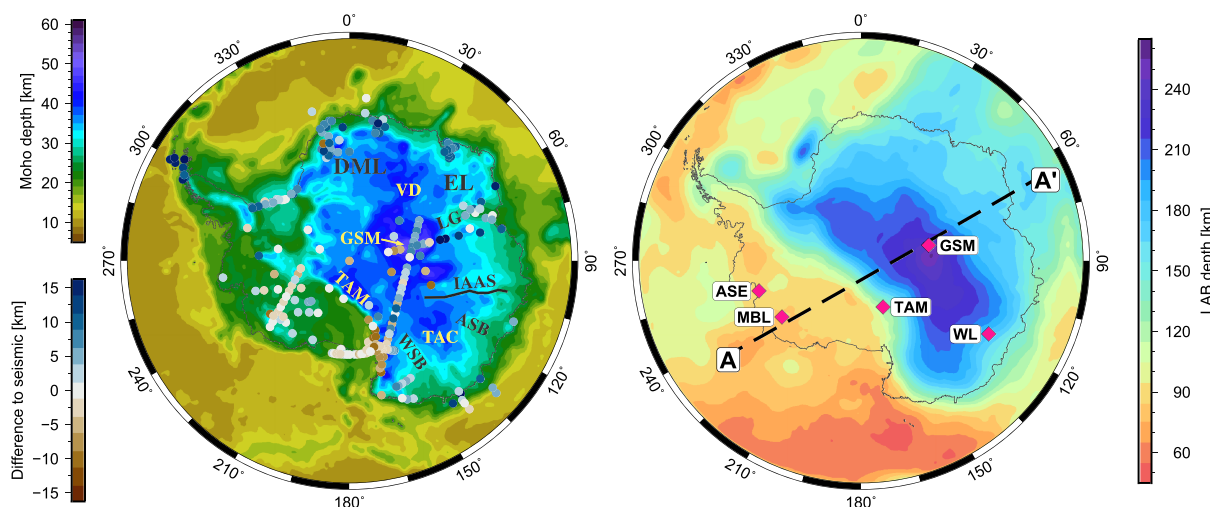


Figure 7. (left) Moho depth of lithospheric model (Model 3). Colored circles show mismatch with respect to seismic estimates from other studies. ASB = Aurora Subglacial Basin, DML = Dronning Maud Land, EL = Enderby Land, GSM = Gamburtsev Subglacial Mountains, IAAS = Indo-Australo-Antarctic Suture, LG = Lambert Graben, TAC = Terre Adélie Craton, TAM = Transantarctic Mountains, VD = Valkyrie Dome, WSB = Wilkes Subglacial Basin. (right) Lithosphere–asthenosphere boundary depth of Model 3. Dashed line A–A' corresponds to temperature cross sections in Figure 8. Pink-colored diamonds indicate locations of vertical temperature profiles in Figure 8.

Another approach to investigate the lithospheric structure of Antarctica in terms of density, along with temperature and composition, has been recently presented by Haeger et al. (2019). Instead of predefining the lithospheric mantle composition, that study inverts for composition, density, and temperature while different seismological *S* wave tomography models are used to iteratively reconcile the estimates in a thermodynamically consistent way. The main difference with our strategy is, however, that Haeger et al. (2019) base their analysis on a predefined Moho depth, whereas it is a model result in our study. Vice versa, we predefine lithospheric mantle compositions in our modeling, while Haeger et al. (2019) invert for these. The degree of depletion of the lithospheric mantle material is strongly dependent on the selection of the seismic tomography model in the inversion of Haeger et al. (2019), demonstrating the need for more seismological surveys for Antarctica.

5.3. Crustal Thickness

The depths of Moho and LAB result from fitting the elevation (Models 1 and 2) and the gravity gradients (Model 3), respectively, starting from the initial model based on the seismologically derived geometry from An et al. (2015a, 2015b). We do not fit our model to seismic data but compare our results with seismic-inferred Moho depth estimates. A considerable number of local seismic Moho depth estimates exist, even though large gaps in the coverage of the Antarctic continent are still present.

Recent continental-scale Moho depth models (e.g., An et al., 2015a; Baranov & Morelli, 2013; Haeger et al., 2019) made use of the local Moho studies by application of different techniques to infer the crustal thickness in poorly covered areas. Several other Moho depth models exist for Antarctica, which are, however, less suited for the evaluation of our model since they involve the inversion of gravity data (e.g., Baranov et al., 2018; Block et al., 2009; O'Donnell & Nyblade, 2014) or only provide estimates in a limited region (e.g., Chaput et al., 2014; Shen et al., 2018; White-Gaynor et al., 2019). In comparison, some of these models show large discrepancies of more than 10 km in large areas of Antarctica (see Pappa et al., 2019, for detailed discussion).

We evaluate the Moho depth of our models at the same seismic stations that have been used by An et al. (2015a) and Baranov and Morelli (2013). Figure 7 shows the Moho depth of Model 3 together with the mismatch to the seismic estimates indicated by colored circles. (For a mismatch histogram see Figure S10.) Parameter and compositional changes from Model 1 to Models 2 and 3 improved the fit in Moho depth for WANT and TAM significantly owing to higher densities in the middle and lower crust. The crustal root beneath areas with high topography is therefore less pronounced. The changes of Moho depth related to the release from isostatic equilibrium from Model 2 to Model 3 are minor in WANT, but in EANT the crust of

Model 3 is thinned compared to Model 2. Areas of relatively thick crust become more pronounced, for instance, in eastern DML, in Terre Adélie, and west of Lake Vostok.

The RMS misfit at the seismic depth points increased slightly from 6.1 km in Model 2 to 6.9 km in Model 3 (Figure S10). It is difficult to quantify the uncertainty of our Moho depth model in relation to the seismic estimates since disagreements exist between studies even at the same locations (Pappa et al., 2019). As a measure of discrepancy, one can calculate the deviation D of the RMS misfit M of our model (6.9 km) from the supposed uncertainty U of seismological methods of ~ 3 km (e.g., Hansen et al., 2009) by

$$D = \sqrt{M^2 - U^2}, \quad (6)$$

which gives 6.2 km. This is, however, a measure of deviation in terms of seismic Moho depth estimates, whereas the misfit of the gravity gradients and the topography must also be taken into account.

The Moho depth of our final Model 3 (Figure 7) exhibits detailed patterns in EANT, typical of gravity-based or Airy-isostatic models (e.g., Block et al., 2009; O'Donnell & Nyblade, 2014; Pappa et al., 2019). Although the AN1-Moho model was used as starting value, distinct differences exist in our Moho depth. DML shows more variations and can be divided into three parts: (1) the northern mountain ranges with crustal roots that exhibits crustal thicknesses of $\sim 40\text{--}45$ km, (2) further south western DML with a rather thin crust of ~ 30 km, and (3) eastern DML as a block with markedly thicker crust of ~ 40 km. These values and the according subdivision are consistent with results from Riedel et al. (2012, 2013), who jointly interpreted aeromagnetic and aerogravity measurements with isostatic modeling of the region. Studies relying on gravity or a combination of both gravity and seismology also show thicker crust in eastern DML (Baranov et al., 2018; Block et al., 2009; O'Donnell & Nyblade, 2014), and this is also revealed by the Rayleigh wave-derived model from An et al. (2015a). However, in previous Moho depth compilations (Baranov & Morelli, 2013), based on regional surveys, the opposite was found with thicker crust in western DML. Yet as no seismic measurements for eastern DML were used in that compilation, the thickness values are interpolated in this area and thus subject to uncertainty.

In the AN1 model, a pronounced small patch of very thick crust beneath the Valkyrie Dome (also referred to as Dome Fuji) is present, but no such feature exists in our results. Instead, the crust there is thinner than at its surroundings.

Only scarce data exist for Enderby Land further east as well. While crustal thickness estimates exist for west Enderby Land (Miyamachi et al., 2003; Yoshii et al., 2004) and the Lambert Graben area (e.g., Feng et al., 2014; Reading, 2006), the interior structure of Enderby Land remains seismically underexplored. Satellite gravity inversions estimate the Moho depth in this region at ~ 40 km (Baranov et al., 2018; Block et al., 2009; O'Donnell & Nyblade, 2014) but can only give a rather blurred image due to the long-wavelength signal. As the gravity gradients enhance shorter wavelengths, which correspond to shallower structures, and our modeling process considers the principle of isostasy, we are able to infer more details in the crustal structure of Enderby Land. West of the Lambert Graben, the Moho is less than 40 km deep, reaching 30 km in central Enderby Land and near the coast. We can also see a clear boundary toward eastern DML along the $\sim 30^\circ\text{N}$ meridian. This is broadly consistent with the models from An et al. (2015a) and O'Donnell and Nyblade (2014).

The GSM, which are adjacent to the southern part of Enderby Land, have been subject to extensive investigations (e.g., An et al., 2016; Ferraccioli et al., 2011; Hansen et al., 2010; Heeszel et al., 2013; Lloyd et al., 2013; Paxman et al., 2016). Yet their formation remains unclear. One hypothesis that has been put forward to explain their uplift is Permian to Cretaceous rifting and strike-slip faulting followed by Cenozoic peak uplift due to fluvial and glacial erosion (Ferraccioli et al., 2011; Paxman et al., 2016; Rose et al., 2013) combined with remarkably low erosion rates (Cox et al., 2010). The remarkably thick crust that is still preserved beneath the GSM has been related to subduction and collision during the late stages of the Pan-African orogenic cycle ($\sim 550\text{--}500$ Ma) by An et al. (2015a) or to much older Grenvillian-age accretion and possible collision of terranes against the composite Archean to Mesoproterozoic Mawson Craton by Ferraccioli et al. (2011). Estimates of crustal root depth values range from more than 60 km in seismic studies (An et al., 2016, 2015a) to ~ 50 km (O'Donnell & Nyblade, 2014; von Frese et al., 2009) or less (Block et al., 2009) in

gravity-based models. Ferraccioli et al. (2011) have shown, based on gravity modeling, that the density contrast between the crustal root of the GSM and the underlying lithospheric upper mantle may be only about 55 kg/m^3 . More generally, An et al. (2015a) conclude that the density contrast for whole EANT is small from comparison of their seismic crustal thickness estimates and an Airy-isostatic Moho depth model. In our model the Moho shows a maximum depth of 52 km, and the root beneath the GSM is elongated in a south-north direction, rather than the more circular-shaped geometry imaged by An et al. (2015a). Between the GSM and the Vostok Highlands to the east, which again are underlain by a thick crust of more than 40 km, a clear lineament of thinner crust is apparent, consistent with seismological estimates (Ramirez et al., 2016) and the location of the proposed eastern branch of the East Antarctic Rift System (Ferraccioli et al., 2011).

Further east we can identify a prominent lineament in the region of the proposed Indo-Australo-Antarctic Suture (Aitken et al., 2014), where Indo-Antarctica and Australo-Antarctica may have collided either during the late Mesoproterozoic assembly of interior EANT or as late as the early Cambrian (Boger, 2011; Collins & Pisarevsky, 2005). However, the exact location of this inferred suture zone cannot precisely be determined from our model. The Terre Adélie Craton stands out as a block of ~40-km-thick crust, consistent with receiver function analyses (Lamarque et al., 2015). It is surrounded by the Aurora Subglacial Basin to the west, the Sabrina Subglacial Basin to the northwest, and the Wilkes Subglacial Basin to the west, which all are characterized by a rather shallow Moho at 30 km or shallower. This level of detail in crustal thickness variation has not been imaged in the region of Wilkes Land so far.

5.4. Lithospheric Thickness

As mentioned before, different definitions of the LAB exist corresponding to different geological understanding and geophysical methods. In our model the LAB is described by a thermal ($1315 \text{ }^\circ\text{C}$ isotherm), rheological (base of rigid layer), and a compositional boundary. Basic assumptions in our modeling, such as composition and crustal rock parameters, imply some uncertainty due to the lack of reliable local constraints. As expressed previously, it should also be noted that the depths of the Moho and the LAB in our models are nonunique, which is always the case in models based on gravity, particularly because the density change at the LAB is generally small. Nevertheless, there are additional aspects that help to constrain the total lithospheric thickness in our model, which are the self-consistent computation of density due to pressure, temperature, and composition as well as the principle of isostasy. Some information about the robustness of the results can be given by the comparison with the seismologically derived and thus gravity-independent LAB depth model AN1-LAB (An et al., 2015b).

An et al. (2015b) used a mixed LAB definition. They converted the S wave velocity model AN1-VS into temperatures and defined the LAB as $1330 \text{ }^\circ\text{C}$ isotherm. The authors state that the vertical resolution of their seismological LAB should be smaller than 20–50 km. This estimation, however, does not include the uncertainties in the conversion of velocities into temperature due to the choice of composition, grain size, and water content, which An et al. (2015b) assume to be ~ $150 \text{ }^\circ\text{C}$. Since both our LAB and the AN1-LAB model are likewise defined as isotherms that only differ by 15 K, we can compare the depths of the LAB (Figures 4 and 7). Although we used the AN1-LAB as a starting geometry, the final LAB of our model results from a completely different methodology. They are markedly similar in most parts of Antarctica, and the differences are mainly within the range of uncertainty of different methods to assess the LAB depth. Similar to An et al. (2015b) and other seismological studies (e.g., Ritzwoller et al., 2001; Schaeffer & Lebedev, 2013), the lithospheric thickness of our final Model 3 shows a strong contrast between WANT where values less than 100 km are attained and EANT with more than 150 km. While the LAB topography in our model is rather smooth within both parts of the continent, the transition is very steep, spanning about 100-km depth difference over 250-km horizontal distance. In WANT few regions show a lithosphere thinner than 80 km, such as MBL, Ellsworth Land, and the Ross Sea front of the TAM. However, we see that a very deep LAB of ~180 km beneath the Weddell Sea emerged in our model, which is not shown by seismological models. This could be a consequence of an overestimated sediment thickness in this area due to the ambiguity of the depth to basement estimates from magnetic data, although notably the presence of cratonic lithosphere beneath the southern part of the Weddell Sea Rift has also been inferred from aeromagnetic studies (e.g., Jordan et al., 2017, and references therein).

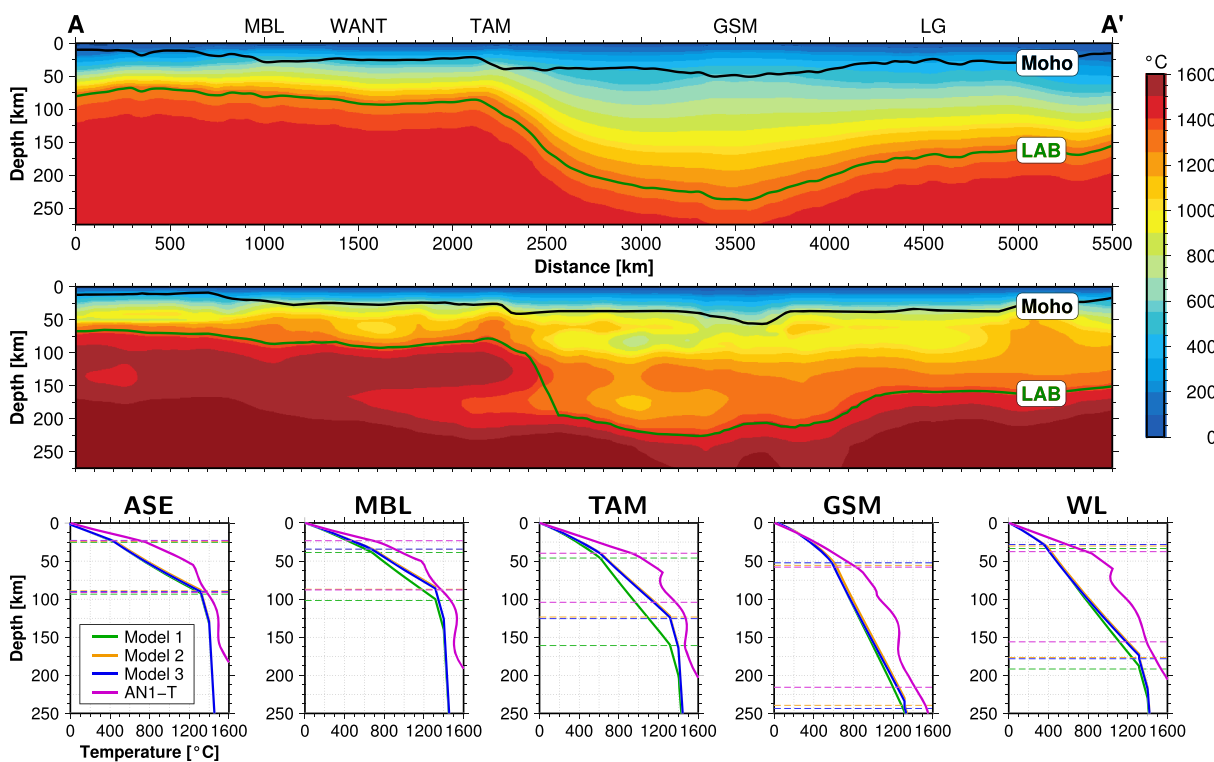


Figure 8. Cross sections show temperature of Model 3 (top) and AN1-T (below) model from An et al. (2015b). (bottom) Vertical temperature profiles for selective locations demonstrate the generally higher temperature estimates from conversion from seismic velocity model (AN1-T). The locations of all profiles are indicated in Figure 7 (right). Horizontal dashed lines indicate depth of Moho and lithosphere-asthenosphere boundary, respectively. Note that the Models 1, 2, and 3 feature steady-state temperature fields and thus do not include thermal anomalies.

In EANT the cratonic nature is clearly reflected by a thick lithospheric root down to ~260-km depth beneath the GSM. Thickness values more than 200 km extend westward to the Pensacola Mountains and the Shackleton Range. To the east we still see 200-km LAB depth beneath George V Land and Wilkes Land. Notably, the lithosphere thins more rapidly toward the coast between the longitudes 20°W and 90°E, reaching 150 km beneath Enderby Land and 100 km beneath western DML, respectively.

A major difference between our model and the AN1-LAB is the lithospheric thickness in the GSM region. In contrast to the AN1-LAB, all our models result in a deeper LAB below the GSM in order to compensate the topographic load. The thickest lithosphere in the AN1 model with more than 230 km is located east of the GSM, whereas in our models the deepest point lies beneath them at ~260 km. An et al. (2015a) regard the different locations of the thickest crust and the deepest LAB in their models to be evidence for a collision belt from the amalgamation of Gondwana during the Pan-African orogeny (~550–500 Ma). Low erosion rates for at least over 250 Myr (Cox et al., 2010) support the hypothesis that the high topography of the GSM might have been stable for 500 Myr. However, the whole mass column must have stayed close to isostatic equilibrium for this scenario. In our model a very thick (thus cold and dense) lithosphere is required to compensate the thick (less dense) crust beneath the GSM. If the crust is even thicker, as seen by An et al. (2015a), and the LAB less deep, isostatic equilibrium could only be achieved by higher densities within the lithosphere, meaning cold temperatures and possibly enriched mantle composition. Yet our model is even colder than AN1-T. It therefore seems unlikely that a thinner and warmer, thus more buoyant, lithosphere could have maintained isostatic equilibrium in the GSM region for several hundreds of million years.

5.5. Thermal Structure and GIA Response

Following our discussion on crustal and lithosphere thickness variations here, we infer the steady-state temperature distribution within the lithosphere and the sublithospheric mantle, which allows to estimate

viscosity values for assessing GIA. It should, however, be kept in mind that our models presume that the lithosphere is in isostatic equilibrium and the steady-state temperature field does not include thermal anomalies. We discuss the thermal structure of our models at five selected points of interest (Figure 8): the Amundsen Sea Embayment (ASE), MBL, TAM, GSM, and Wilkes Land. Further comparison is made with the temperature model AN1-T from An et al. (2015b), which results from conversion of the *S* wave velocity model AN1-VS (An et al., 2015a) into temperatures. The authors point out that a homogeneous mantle composition and pressure dependency have been considered in the conversion method but not potential water content or partial melt. They take their estimated mantle temperatures to be the upper bound, and note that if the converted temperatures for the upper mantle seem unreasonably high, a possible explanation might be the existence of melt or fluid inclusions (An et al., 2015b). Indeed, the temperature of the AN1 model is slightly higher than ours, and some areas of increased temperature are not visible in our models.

The cross section in Figure 8 demonstrates the striking temperature variations within the upper mantle between WANT to EANT in both Model 3 and AN1-T. At the transition from WANT to EANT, the AN1 model and our model show high temperatures at the steps of Moho boundary and LAB. Although our model only considers steady-state conditions and thus no thermal anomalies, the temperature at the Moho reaches almost 700 °C. Such values would be generally expected in orogenic belts (McKenzie et al., 2005), while the Moho temperature beneath cratonic shields is estimated to range from 300–500 °C (Archean) to 450–650 °C (Paleoproterozoic; Artemieva, 2009). The generally higher temperatures of the AN1-T model compared to our models, particularly at the crust-mantle boundary, are also visible in the vertical temperature profiles (Figure 8), for example, at the TAM profile. Here, the AN1-T temperatures not only are ~400 K higher in the middle part of the mantle lithosphere (~70-km depth), but also our models differ from each other due to variations in lithospheric thickness. The lithosphere is much thinner (~125 km) in Models 2 and 3 than in Model 1 (>150 km). Consequently, the temperature is higher within the lithosphere in Models 2 and 3 and approximately 200 K higher at 125-km depth. Due to the associated density decrease in the mantle, this generally allows a thinner crust to be in isostatic balance and does not require a pronounced crustal root. A substantially hotter mantle could potentially increase this effect to the extent that a much thinner crust can overcompensate the topographic load. The cross section (Figure 8) also shows the lateral temperature variation of the uppermost lithospheric mantle between the TAM and the region beneath the GSM. Beneath the TAM, temperatures are high throughout the lithosphere due to the shallow LAB. The hinterland of the TAM toward the GSM features rather low temperatures below the relatively thin crust, whereas temperatures rise again beneath the GSM's crustal root. **Here the thick crust provides additional heat from radiogenic decay, which is higher than in the mantle due to the increased abundance of uranium, thorium, and potassium.** Such temperature variations affect the upper mantle seismic velocities, leading to velocity highs in regions of low temperature and a velocity low beneath the GSM. Such decreased velocities have been observed by Shen et al. (2018), who, however, hypothesize that they originate from compositional changes. Beneath the GSM, our models show ~600 °C at the Moho, whereas AN1-T suggests ~800 °C, which is much higher than generally expected for cratonic shields. Varying crustal density parameters in our Models 2 and 3 with respect to Model 1 in the GSM region apparently have no significant effect on the temperature. The same phenomenon occurs in the profile for Wilkes Land, where the impact of the implementation of Archean lithospheric mantle on the temperature is also minor, whereas it has a significant effect on the density.

In the ASE in WANT, our models show almost identical values, whereas the Moho in the AN1-T model is more than 200 K hotter and exceeds 700 °C. On the other hand, all models have similar temperatures at the lithospheric base. In the sublithospheric mantle the *S* wave inferred temperatures of the AN1 model show a pronounced temperature increase with respect to our models beneath the ASE. This is consistent with observations of the short-term interaction between solid Earth movement and ice mass changes in the ASE, which suggest very low upper mantle viscosities (Barletta et al., 2018). It is also consistent with seismic low-velocity zones in other studies (Hansen et al., 2014; Shen et al., 2018). Our models may underestimate the temperature because they represent a steady-state temperature distribution with a lithosphere in isostatic equilibrium, which might not be the case in the ASE. Similar limitations may apply for MBL. Here, the changes in crustal parameters from Model 1 to Model 2 led to a shallower Moho and LAB, resulting in higher temperatures within the lithosphere. As a consequence, lower densities and seismic velocities can be expected. However, seismological studies inferred significant mantle velocity reduction

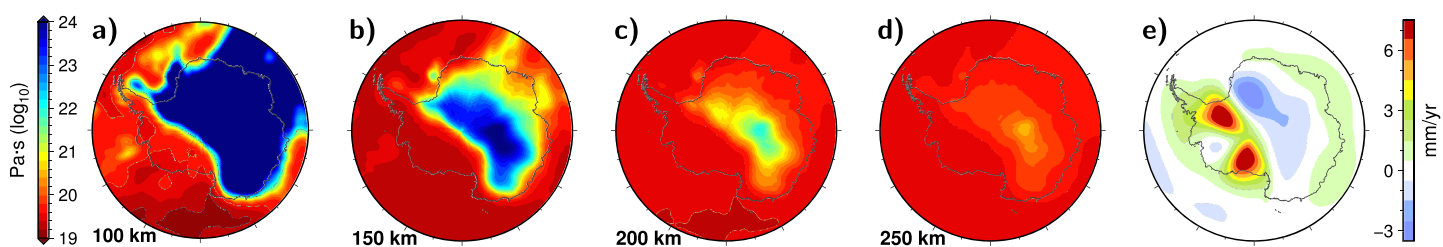


Figure 9. Modeled mantle viscosity (a–d) and resulting uplift rates (e) in a dry olivine rheology and 4-mm grain size scenario. The depth slices represent values at 100 (a), 150 (b), 200 (c), and 250 km (d).

of 1–3% for P waves and 2–5% for S waves beneath MBL (Hansen et al., 2014; Heeszel et al., 2016; Lloyd et al., 2015; Shen et al., 2018; White-Gaynor et al., 2019), accompanied by Cenozoic volcanism (e.g., LeMasurier, 1990). Such velocity anomalies would correspond to a temperature increase of \sim 150 K (Lloyd et al., 2015). If, on the other hand, the upper mantle beneath MBL has an elevated water content compared to surrounding areas, which could likely be the case due to a history of subduction in the region (LeMasurier et al., 2016), then partial melts could cause the decrease in seismic velocities (White-Gaynor et al., 2019).

The temperature field does not only affect rock densities and hence contribute to isostasy but, in general, also controls dynamic effects, such as GIA and mantle convection, in which viscosity is the crucial property. Temperature or viscosity can be derived from seismic velocity anomalies, yet with large uncertainty (Ivins & Sammis, 1995). Here we take the 3-D temperature values from our thermodynamically self-consistent model to derive mantle viscosities and point out the implications for present-day uplift rates in Antarctica, which can be compared with GPS measurements to ultimately constrain past ice thickness.

Viscosity values are computed according to equation (4) with temperatures from Model 3. As stated in section 3, we compute viscosity for dry olivine rheology and 4-mm grain size (Figure 9). As a result, viscosity at 100-km depth in all of EANT is so high that it is effectively elastic and can thus be considered as part of the lithosphere for GIA models. The viscosity in WANT is somewhat higher than found in earlier studies (Barletta et al., 2018; Bradley et al., 2015; van der Wal et al., 2015). Using wet rheology lowers viscosity to around 10^{18} Pa·s for large parts of WANT, in agreement with viscosity for water-saturated peridotite provided in O'Donnell et al. (2017). Lowering the grain size to 1 mm even reduces viscosity in WANT to below 10^{18} Pa·s. This corresponds to relaxation times in the order of decades. For these small relaxation times, the solid Earth response to changes in loading thousands of years ago will have reached equilibrium.

Uplift rates in Figure 9e show two maxima in location of former ice domes in the W12 ice history model. GPS uplift rates (Argus et al., 2014; Thomas et al., 2011) and empirical GIA models (Martin-Español et al., 2017) prefer somewhat smaller values, but note that no measurements are available in the locations of maximum uplift rates. Smaller uplift rates can be achieved with lower grain size (1 mm) or a wet rheology in our model, but these viscosities result in uplift rates of less than 1 mm/year, which is well below observed values. However, this argument rests on the assumption that all ice loading changes are accounted for, while Antarctic-wide ice loading histories such as the W12 model used in this study do not include changes in ice sheet thickness that occurred in the last centuries, and the response to those changes is absent from Figure 9e. A low viscosity in combination with recent ice unloading could produce significant uplift rates. The lowest viscosities obtained for the wet and small grain size rheologies are also below those inferred from observations of late Holocene ice loading relaxation, including in Iceland (Barnhoorn et al., 2011; Sigmundsson, 1991) and parts of Antarctica (Barletta et al., 2018). Based on this, our preferred model features the dry rheology and 4-mm grain size. The preference for GIA observations for dry rheology is subject to the uncertainties introduced by applying the olivine flow law to the upper mantle rheology deficiencies in the experimental flow law itself and our temperature model. From a petrology point of view, a completely dry rheology is plausible. The upper mantle contains on average small amounts of water (50–200 ppm; Hirschmann, 2006). Low hydration in WANT is supported by magnetotelluric measurements (Wannamaker et al., 2017) and suggested for cratons such as EANT (Peslier et al., 2010). However,

possible hydration due to recent subduction in WANT (Emry et al., 2015) and the variation in flow law parameters in xenolith findings across Antarctica (see table in van der Wal et al., 2015) suggest the necessity of regional modeling of flow law parameters.

6. Conclusions

A comprehensive and self-consistent continental-scale model of Antarctica's lithosphere is presented in this study. Satellite gravity gradient data, seismological estimates, thermodynamic modeling, and the principle of isostasy are used to infer crustal and lithospheric thickness, density, and temperature distribution. By integrating a variety of geophysical observables and principles, a higher robustness of the result is achieved compared to modeling them separately. A precise quantification of the uncertainties of all individual geophysical properties can, however, not be obtained because the model is too computationally expensive to follow a probabilistic approach. Integrated and probabilistic modeling methods of the lithosphere are currently in development yet still in 1-D and immature (Afonso et al., 2016). Before applying them on poorly explored areas like Antarctica, they need to give proof of their reliability and robustness.

Our new Moho depth map provides higher-resolution estimates for poorly surveyed regions of EANT, where seismic station coverage is sparse or nonexistent. We find that ~30- to 35-km-thick crust is present in Wilkes Land, while the Terre Adélie Craton features distinctly thicker (~40 km thick) crust. The GSM are underlain by a marked crustal root with a ~52-km-deep Moho. Although our model cannot solve the debate about the origin and evolution of the GSM directly, it indicates that a thick and cold and thus dense lithospheric mantle is needed to compensate the thick buoyant crust to maintain isostasy.

The 3-D temperature distribution from our model is taken to infer mantle viscosity and to model present-day uplift rates for Antarctica due to GIA. Viscosity values are computed for dry olivine rheology and moderate grain size (4 mm). High viscosities imply that the GIA lithosphere is at least 100 km thick in EANT, and below 150 km in its central part. In WANT, viscosity values are around 10^{19} Pa·s, slightly above previously published values. Lowering grain size or assuming wet rheology results in uplift rates well below measured values. Our modeling prefers a dry rheology and a moderate grain size. A limitation of this estimation is, however, the absence of ice thickness variations during the last centuries in the used W12 model. Recent unloading together with low viscosity values could have a strong impact on present-day uplift rates. Therefore, future studies should include ice thickness changes in the last decades and centuries as well as 3-D variations and rheologic parameters below 400-km depth to estimate the full dynamic effect due to glacial loading.

Acknowledgments

This study was carried out in the course of the projects GOCE + Antarctica and 3-D Earth. Both projects have been funded by the European Space Agency (ESA) as a Support to Science Element. We thank Eva Bredow for her kind support with earlier versions of the manuscript. Pippa Whitehouse is acknowledged for making available the W12 ice history (Whitehouse et al., 2012). Our special thanks go to J. P. O'Donnell, Doug Wiens, and one anonymous reviewer for their constructive contribution and criticism. All grid files and maps were created using Generic Mapping Tools (GMT) Version 5 (Wessel et al., 2013), partly making use of color maps from Fabio Crameri (2018). Other data, models, and modeling software used in this study have been obtained from Amante and Eakins (2009), An et al. (2015a, 2015b), Bouman et al. (2016), Connolly (2005), Fretwell et al. (2013), Fuller et al. (2009), Garcia-Castellanos (2002), Golynsky et al. (2001), Uieda et al. (2011), Whittaker et al. (2013), and Wobbe et al. (2014). Our modeling results can be found in the supporting information and will also be available for download from the project website (<https://www.bas.ac.uk/project/goceanarctica/>).

References

- Afonso, J. C., Fernández, M., Ranalli, G., Griffin, G., & Connolly, J. A. D. (2008). Integrated geophysical-petrological modeling of the lithosphere and sublithospheric upper mantle: Methodology and applications. *Geochemistry, Geophysics, Geosystems*, 9, Q05008. <https://doi.org/10.1029/2007GC001834>
- Afonso, J. C., Fullea, J., Griffin, W. L., Yang, Y., Jones, A. G., Connolly, D., & O'Reilly, S. Y. (2013). 3-D multiobservable probabilistic inversion for the compositional and thermal structure of the lithosphere and upper mantle. I: A priori petrological information and geophysical observables. *Journal of Geophysical Research: Solid Earth*, 118, 2586–2617. <https://doi.org/10.1002/jgrb.50124>
- Afonso, J. C., Moorkamp, M., & Fullea, J. (2016). Imaging the lithosphere and upper mantle. In M. Moorkamp, P. G. Lelièvre N. Linde & A. Khan (Eds.). *Integrated Imaging of the Earth* (pp. 191–218). American Geophysical Union (AGU). <https://doi.org/10.1002/9781118929063.ch10>
- Afonso, J. C., Ranalli, G., & Fernández, M. (2007). Density structure and buoyancy of the oceanic lithosphere revisited. *Geophysical Research Letters*, 34, L10302. <https://doi.org/10.1029/2007GL029515>
- Atkin, A. R. A., Young, D. A., Ferraccioli, F., Betts, P. G., Greenbaum, J. S., Richter, T. G., et al. (2014). The subglacial geology of Wilkes Land, East Antarctica. *Geophysical Research Letters*, 41, 2390–2400. <https://doi.org/10.1002/2014GL059405>
- Amante, C., & Eakins, B. W. (2009). ETOP01 1 arc-minute global relief model: Procedures, data sources and analysis. *National Geophysical Data Center, NOAA*. <https://doi.org/10.7289/V5C8276M>
- An, M., Wiens, D. A., & Zhao, Y. (2016). A frozen collision belt beneath ice: An overview of seismic studies around the Gamburtsev Subglacial Mountains, East Antarctica. *Advances in Polar Science*, 27(2), 78–89. <https://doi.org/10.13679/j.adpvs.2016.2.00078>
- An, M., Wiens, D. A., Zhao, Y., Feng, M., Nyblade, A. A., Kanao, M., et al. (2015a). S-velocity model and inferred Moho topography beneath the Antarctic Plate from Rayleigh waves. *Journal of Geophysical Research: Solid Earth*, 120, 359–383. <https://doi.org/10.1002/2014JB011332>
- An, M., Wiens, D. A., Zhao, Y., Feng, M., Nyblade, A., Kanao, M., et al. (2015b). Temperature, lithosphere–asthenosphere boundary, and heat flux beneath the Antarctic Plate inferred from seismic velocities. *Journal of Geophysical Research: Solid Earth*, 120, 8720–8742. <https://doi.org/10.1002/2015JB011917>

- Argus, D. F., Peltier, W. R., Drummond, R., & Moore, A. W. (2014). The Antarctica component of postglacial rebound model ICE-6G_C (VM5a) based on GPS positioning, exposure age dating of ice thicknesses, and relative sea level histories. *Geophysical Journal International*, 198(1), 537–563. <https://doi.org/10.1093/gji/ggu140>
- Armenti, P., & Perinelli, C. (2010). Cenozoic thermal evolution of lithospheric mantle in northern Victoria Land (Antarctica): Evidences from mantle xenoliths. *Tectonophysics*, 486(1), 28–35. <https://doi.org/10.1016/j.tecto.2010.02.006>
- Artemieva, I. M. (2009). The continental lithosphere: Reconciling thermal, seismic, and petrologic data. *Lithos*, 109(1–2), 23–46. <https://doi.org/10.1016/j.lithos.2008.09.015>
- Baranov, A., & Morelli, A. (2013). The Moho depth map of the Antarctica region. *Tectonophysics*, 609, 299–313. <https://doi.org/10.1016/j.tecto.2012.12.023>
- Baranov, A., Tenzer, R., & Bagherbandi, M. (2018). Combined gravimetric–seismic crustal model for Antarctica. *Surveys in Geophysics*, 39(1), 23–56. <https://doi.org/10.1007/s10712-017-9423-5>
- Barletta, V. R., Bevis, M., Smith, B. E., Wilson, T., Brown, A., Bordoni, A., et al. (2018). Observed rapid bedrock uplift in Amundsen Sea Embayment promotes ice-sheet stability. *Science*, 360(6395), 1335–1339. <https://doi.org/10.1126/science.aao1447>
- Barnhoorn, A., van der Wal, W., Vermeersen, B. L. A., & Drury, M. R. (2011). Lateral, radial, and temporal variations in upper mantle viscosity and rheology under Scandinavia. *Geochemistry, Geophysics, Geosystems*, 12, Q01007. <https://doi.org/10.1029/2010GC003290>
- Barnhoorn, A., van der Wal, W., & Drury, M. R. (2011). Upper mantle viscosity and lithospheric thickness under Iceland. *Journal of Geodynamics*, 52(3), 260–270. <https://doi.org/10.1016/j.jog.2011.01.002>
- Beyer, E. E., Griffin, W. L., & O'Reilly, S. Y. (2006). Transformation of Archaean lithospheric mantle by refertilization: Evidence from exposed peridotites in the Western Gneiss Region, Norway. *Journal of Petrology*, 47(8), 1611–1636. <https://doi.org/10.1093/petrology/egl022>
- Bingham, R. G., Ferraccioli, F., King, E. C., Larter, R. D., Pritchard, H. D., Smith, A. M., & Vaughan, D. G. (2012). Inland thinning of West Antarctic Ice Sheet steered along subglacial rifts. *Nature*, 487, 468.
- Block, A. E., Bell, R. E., & Studinger, M. (2009). Antarctic crustal thickness from satellite gravity: Implications for the Transantarctic and Gamburtsev Subglacial Mountains. *Earth and Planetary Science Letters*, 288(1–2), 194–203. <https://doi.org/10.1016/j.epsl.2009.09.022>
- Boger, S. D. (2011). Antarctica—Before and after Gondwana. *Gondwana Research*, 19(2), 335–371. <https://doi.org/10.1016/j.gr.2010.09.003>
- Borg, S. G., Depaolo, D. J., & Smith, B. M. (1990). Isotopic structure and tectonics of the central Transantarctic mountains. *Journal of Geophysical Research*, 95(B5), 6647–6667. <https://doi.org/10.1029/JB095iB05p06647>
- Bouman, J., Ebbing, J., Fuchs, M., Sebera, J., Lieb, V., Szwilus, W., et al. (2016). Satellite gravity gradient grids for geophysics. *Scientific Reports*, 6(1), 21050. <https://doi.org/10.1038/srep21050>
- Bouman, J., Ebbing, J., Meekes, S., Fattah, R. A., Fuchs, M., Gradmann, S., et al. (2015). GOCE gravity gradient data for lithospheric modeling. *International Journal of Applied Earth Observation and Geoinformation*, 35(Part A), 16–30. <https://doi.org/10.1016/j.jag.2013.11.001>
- Bradley, S. L., Hindmarsh, R. C. A., Whitehouse, P. L., Bentley, M. J., & King, M. A. (2015). Low post-glacial rebound rates in the Weddell Sea due to Late Holocene ice-sheet readvance. *Earth and Planetary Science Letters*, 413, 79–89. <https://doi.org/10.1016/j.epsl.2014.12.039>
- Braitenberg, C., Pettenati, F., & Zadro, M. (1997). Spectral and classical methods in the evaluation of Moho undulations from gravity data: The NE Italian Alps and isostasy. *Journal of Geodynamics*, 23(1), 5–22. [https://doi.org/10.1016/S0264-3707\(96\)00024-5](https://doi.org/10.1016/S0264-3707(96)00024-5)
- Chappell, A., & Kusznir, N. (2008). An algorithm to calculate the gravity anomaly of sedimentary basins with exponential density-depth relationships. *Geophysical Prospecting*, 56(2), 249–258. <https://doi.org/10.1111/j.1365-2478.2007.00674.x>
- Chaput, J., Aster, R. C., Huerta, A., Sun, X., Lloyd, A., Wiens, D., et al. (2014). The crustal thickness of West Antarctica. *Journal of Geophysical Research: Solid Earth*, 119, 378–395. <https://doi.org/10.1002/2013JB010642>
- Collins, A. S., & Pisarevsky, S. A. (2005). Amalgamating eastern Gondwana: The evolution of the Circum-Indian Orogenes. *Earth-Science Reviews*, 71(3–4), 229–270. <https://doi.org/10.1016/j.earscirev.2005.02.004>
- Connolly, J. A. D. (2005). Computation of phase equilibria by linear programming: A tool for geodynamic modeling and its application to subduction zone decarbonation. *Earth and Planetary Science Letters*, 236(1), 524–541.
- Cox, S. E., Thomson, S. N., Reiners, P. W., Hemming, S. R., & van de Flierdt, T. (2010). Extremely low long-term erosion rates around the Gamburtsev Mountains in interior East Antarctica. *Geophysical Research Letters*, 37, L22307. <https://doi.org/10.1029/2010GL045106>
- Craddock, J. P., Schmitz, M. D., Crowley, J. L., Larocque, J., Pankhurst, R. J., Juda, N., et al. (2017). Precise U-Pb zircon ages and geochemistry of Jurassic granites, Ellsworth–Whitmore terrane, central Antarctica. *GSA Bulletin*, 129(1–2), 118–136. <https://doi.org/10.1130/B31485.1>
- Crameri, F. (2018). Geodynamic diagnostics, scientific visualisation and StagLab 3.0. *Geoscientific Model Development*, 11(6), 2541–2562. <https://doi.org/10.5194/gmd-11-2541-2018>
- Dalziel, I. W. D., & Elliot, D. H. (1982). West Antarctica: Problem child of Gondwanaland. *Tectonics*, 1(1), 3–19. <https://doi.org/10.1029/TC001i001p00003>
- Dziewonski, A. M., & Anderson, D. L. (1981). Preliminary reference Earth model. *Physics of the Earth and Planetary Interiors*, 25(4), 297–356. [https://doi.org/10.1016/0031-9201\(81\)90046-7](https://doi.org/10.1016/0031-9201(81)90046-7)
- Eaton, D. W., Derbyshire, F., Evans, R. L., Grüter, H., Jones, A. G., & Yuan, X. (2009). The elusive lithosphere–asthenosphere boundary (LAB) beneath cratons. *Lithos*, 109(1), 1–22.
- Ebbing, J., Haas, P., Ferraccioli, F., Pappa, F., Szwilus, W., & Bouman, J. (2018). Earth tectonics as seen by GOCE—Enhanced satellite gravity gradient imaging. *Scientific Reports*, 8(1), 16356. <https://doi.org/10.1038/s41598-018-34733-9>
- Elliot, D. H., Fanning, C. M., & Hulett, S. R. W. (2015). Age provinces in the Antarctic craton: Evidence from detrital zircons in Permian strata from the Beardmore Glacier region, Antarctica. *Gondwana Research*, 28(1), 152–164. <https://doi.org/10.1016/j.gr.2014.03.013>
- Emry, E. L., Nyblade, A. A., Julià, J., Anandakrishnan, S., Aster, R. C., Wiens, D. A., et al. (2015). The mantle transition zone beneath West Antarctica: Seismic evidence for hydration and thermal upwellings. *Geochemistry, Geophysics, Geosystems*, 16, 40–58. <https://doi.org/10.1002/2014GC005588>
- Feng, M., An, M., An, C., Shi, G., Zhao, Y., Li, Y., & Wiens, D. (2014). Crustal thicknesses along the traverse from Zhongshan to Dome A in Eastern Antarctica. *Chinese Journal of Polar Research*, 26, 177–185. <https://doi.org/10.13679/j.jdyj.2014.2.177>
- Ferraccioli, F., Armadillo, E., Jordan, T., Bozzo, E., & Corr, H. (2009). Aeromagnetic exploration over the East Antarctic Ice Sheet: A new view of the Wilkes Subglacial Basin. *Tectonophysics*, 478(1–2), 62–77. <https://doi.org/10.1016/j.tecto.2009.03.013>
- Ferraccioli, F., & Bozzo, E. (2003). Cenozoic strike-slip faulting from the eastern margin of the Wilkes Subglacial Basin to the western margin of the Ross Sea Rift: An aeromagnetic connection. *Geological Society, London, Special Publications*, 210(1), 109–133. <https://doi.org/10.1144/GSL.SP.2003.210.01.07>

- Ferraccioli, F., Finn, C. A., Jordan, T. A., Bell, R. E., Anderson, L. M., & Damaske, D. (2011). East Antarctic rifting triggers uplift of the Gamburtsev Mountains. *Nature*, 479(7373), 388–392. <https://doi.org/10.1038/nature10566>
- Fitzgerald, P. (2002). Tectonics and landscape evolution of the Antarctic plate since the breakup of Gondwana, with an emphasis on the West Antarctic Rift System and the Transantarctic Mountains. *Royal Society of New Zealand Bulletin*, 35, 453–469.
- Frederick, B. C., Young, D. A., Blankenship, D. D., Richter, T. G., Kempf, S. D., Ferraccioli, F., & Siegert, M. J. (2016). Distribution of subglacial sediments across the Wilkes Subglacial Basin, East Antarctica. *Journal of Geophysical Research: Earth Surface*, 121, 790–813. <https://doi.org/10.1002/2015JF003760>
- Fretwell, P., Pritchard, H. D., Vaughan, D. G., Bamber, J. L., Barrand, N. E., Bell, R., et al. (2013). Bedmap2: Improved ice bed, surface and thickness datasets for Antarctica. *The Cryosphere*, 7(1), 375–393. <https://doi.org/10.5194/tc-7-375-2013>
- Fullea, J., Afonso, J. C., Connolly, J. A. D., Fernández, M., Garcia-Castellanos, D., & Zeyen, H. (2009). LitMod3D: An interactive 3-D software to model the thermal, compositional, density, rheological and seismological structure of the lithosphere and sublithospheric upper mantle. *Geochemistry, Geophysics, Geosystems*, 10, Q08019. <https://doi.org/10.1029/2009GC002391>
- Fullea, J., Lebedev, S., Agius, M. R., Jones, A. G., & Afonso, J. C. (2012). Lithospheric structure in the Baikal–central Mongolia region from integrated geophysical–petrological inversion of surface-wave data and topographic elevation. *Geochemistry, Geophysics, Geosystems*, 13, Q0AK09. <https://doi.org/10.1029/2012GC004138>
- Fullea, J., Rodríguez-González, J., Charco, M., Martínez, Z., Negredo, A., & Villaseñor, A. (2015). Perturbing effects of sub-lithospheric mass anomalies in GOCE gravity gradient and other gravity data modelling: Application to the Atlantic-Mediterranean transition zone. *International Journal of Applied Earth Observation and Geoinformation*, 35(Part A), 54–69. <https://doi.org/10.1016/j.jag.2014.02.003>
- Garcia-Castellanos, D. (2002). Interplay between lithospheric flexure and river transport in foreland basins. *Basin Research*, 14(2), 89–104. <https://doi.org/10.1046/j.1365-2117.2002.00174.x>
- Golynsky, A., Chiappini, M., Damaske, D., Ferraccioli, F., Ferris, J., Finn, C., et al. (2001). In P. Morris & R. von Frese (Eds.), *ADMAP—Magnetic anomaly map of the Antarctic*. Cambridge: British Antarctic Survey.
- Golynsky, A. V., Ferraccioli, F., Hong, J. K., Golynsky, D. A., von Frese, R. R. B., Young, D. A., et al. (2018). New magnetic anomaly map of the Antarctic. *Geophysical Research Letters*, 45, 6437–6449. <https://doi.org/10.1029/2018GL078153>
- Goodge, J. W., & Fanning, C. M. (2016). Mesoarchean and Paleoproterozoic history of the Nimrod Complex, central Transantarctic Mountains, Antarctica: Stratigraphic revisions and relation to the Mawson Continent in East Gondwana. *Precambrian Research*, 285, 242–271. <https://doi.org/10.1016/j.precamres.2016.09.001>
- Graw, J. H., & Hansen, S. E. (2017). Upper mantle seismic anisotropy beneath the Northern Transantarctic Mountains, Antarctica from PKS, SKS, and SKKS splitting analysis. *Geochemistry, Geophysics, Geosystems*, 18, 544–557. <https://doi.org/10.1002/2016GC006729>
- Hansen, S. E., Julià, J., Nyblade, A. A., Pyle, M. L., Wiens, D. A., & Anandakrishnan, S. (2009). Using S wave receiver functions to estimate crustal structure beneath ice sheets: An application to the Transantarctic Mountains and East Antarctic craton. *Geochemistry, Geophysics, Geosystems*, 10, Q08014. <https://doi.org/10.1029/2009GC002576>
- Haeger, C., Kaban, M. K., Tesauro, M., Petrunin, A. G., & Mooney, W. D. (2019). 3-D Density, thermal, and compositional model of the Antarctic lithosphere and implications for its evolution. *Geochemistry, Geophysics, Geosystems*, 20, 688–707. <https://doi.org/10.1029/2018GC008033>
- Hansen, S. E., Graw, J. H., Kenyon, L. M., Nyblade, A. A., Wiens, D. A., Aster, R. C., et al. (2014). Imaging the Antarctic mantle using adaptively parameterized P-wave tomography: Evidence for heterogeneous structure beneath West Antarctica. *Earth and Planetary Science Letters*, 408, 66–78. <https://doi.org/10.1016/j.epsl.2014.09.043>
- Hansen, S. E., Kenyon, L. M., Graw, J. H., Park, Y., & Nyblade, A. A. (2016). Crustal structure beneath the Northern Transantarctic Mountains and Wilkes Subglacial Basin: Implications for tectonic origins. *Journal of Geophysical Research: Solid Earth*, 121, 812–825. <https://doi.org/10.1002/2015JB012325>
- Hansen, S. E., Nyblade, A. A., Heeszel, D. S., Wiens, D. A., Shore, P., & Kanao, M. (2010). Crustal structure of the Gamburtsev Mountains, East Antarctica, from S-wave receiver functions and Rayleigh wave phase velocities. *Earth and Planetary Science Letters*, 300(3–4), 395–401. <https://doi.org/10.1016/j.epsl.2010.10.022>
- Harley, S. L., Fitzsimons, I. C. W., & Zhao, Y. (2013). Antarctica and supercontinent evolution: historical perspectives, recent advances and unresolved issues. *Geological Society, London, Special Publications*, 383(1), 1–34. <https://doi.org/10.1144/SP383.9>
- Heeszel, D. S., Wiens, D. A., Anandakrishnan, S., Aster, R. C., Dalziel, I. W. D., Huerta, A. D., et al. (2016). Upper mantle structure of central and West Antarctica from array analysis of Rayleigh wave phase velocities. *Journal of Geophysical Research: Solid Earth*, 121, 1758–1775. <https://doi.org/10.1002/2015JB012616>
- Heeszel, D. S., Wiens, D. A., Nyblade, A. A., Hansen, S. E., Kanao, M., An, M., & Zhao, Y. (2013). Rayleigh wave constraints on the structure and tectonic history of the Gamburtsev Subglacial Mountains, East Antarctica. *Journal of Geophysical Research: Solid Earth*, 118, 2138–2153. <https://doi.org/10.1002/jgrb.50171>
- Hemingway, D. J., & Matsuyama, I. (2017). Isostatic equilibrium in spherical coordinates and implications for crustal thickness on the Moon, Mars, Enceladus, and elsewhere. *Geophysical Research Letters*, 44, 7695–7705. <https://doi.org/10.1002/2017GL073334>
- Hirschmann, M. M. (2006). Water, melting, and the deep Earth H₂O cycle. *Annual Review of Earth and Planetary Sciences*, 34(1), 629–653. <https://doi.org/10.1146/annurev.earth.34.031405.125211>
- Hirt, C., Kuhn, M., Featherstone, W. E., & Göttl, F. (2012). Topographic/isostatic evaluation of new-generation GOCE gravity field models. *Journal of Geophysical Research*, 117, B05407. <https://doi.org/10.1029/2011JB008878>
- Hirth, G., & Kohlstedt, D. (2003). Rheology of the upper mantle and the mantle wedge: A view from the experimentalists. In J. Eiler (Eds.). *Inside the Subduction Factory* (pp. 83–105). American Geophysical Union (AGU). <https://doi.org/10.1029/138GM06>
- Hofmeister, A. M. (1999). Mantle values of thermal conductivity and the geotherm from phonon lifetimes. *Science*, 283(5408), 1699–1706. <https://doi.org/10.1126/science.283.5408.1699>
- Holzrichter, N., & Ebbing, J. (2016). A regional background model for the Arabian Peninsula from modeling satellite gravity gradients and their invariants. *Tectonophysics*. <https://doi.org/10.1016/j.tecto.2016.06.002>
- Irfune, T., & Ringwood, A. E. (1987). Phase transformations in a harzburgite composition to 26 GPa: Implications for dynamical behaviour of the subducting slab. *Earth and Planetary Science Letters*, 86(2), 365–376. [https://doi.org/10.1016/0012-821X\(87\)90233-0](https://doi.org/10.1016/0012-821X(87)90233-0)
- Ivins, E. R., & Sammis, C. G. (1995). On lateral viscosity contrast in the mantle and the rheology of low-frequency geodynamics. *Geophysical Journal International*, 123(2), 305–322. <https://doi.org/10.1111/j.1365-246X.1995.tb06856.x>
- Ji, S., & Zhao, P. (1994). Layered rheological structure of subducting oceanic lithosphere. *Earth and Planetary Science Letters*, 124(1), 75–94. [https://doi.org/10.1016/0012-821X\(94\)00085-9](https://doi.org/10.1016/0012-821X(94)00085-9)
- Jokat, W., & Herter, U. (2016). Jurassic failed rift system below the Filchner-Ronne-Shelf, Antarctica: New evidence from geophysical data. *Tectonophysics*, 688, 65–83. <https://doi.org/10.1016/j.tecto.2016.09.018>

- Jones, A. G., Afonso, J. C., Fullea, J., & Salajegheh, F. (2014). The lithosphere–asthenosphere system beneath Ireland from integrated geophysical–petrological modeling—I: Observations, 1D and 2D hypothesis testing and modeling. *Lithos*, 189, 28–48. <https://doi.org/10.1016/j.lithos.2013.10.033>
- Jordan, T. A., Ferraccioli, F., & Leat, P. T. (2017). New geophysical compilations link crustal block motion to Jurassic extension and strike-slip faulting in the Weddell Sea Rift System of West Antarctica. *Gondwana Research*, 42, 29–48. <https://doi.org/10.1016/j.gr.2016.09.009>
- Lamarque, G., Barruol, G., Fontaine, F. R., Bascou, J., & Ménot, R.-P. (2015). Crustal and mantle structure beneath the Terre Adélie Craton, East Antarctica: Insights from receiver function and seismic anisotropy measurements. *Geophysical Journal International*, 200(2), 807–821. <https://doi.org/10.1093/gji/ggu430>
- LeMasurier, W. E. (1990). Late Cenozoic volcanism on the Antarctic plate: An overview. In W. LeMasurier, J. Thomson, P. Baker, P. Kyle, P. Rowley, J. Smellie, & W. Verwoerd (Eds.). *Volcanoes of the Antarctic Plate and Southern Oceans* (pp. 1–17). American Geophysical Union (AGU). <https://doi.org/10.1029/AR048p0001>
- LeMasurier, W. E., Choi, S. H., Hart, S. R., Mukasa, S., & Rogers, N. (2016). Reconciling the shadow of a subduction signature with rift geochemistry and tectonic environment in Eastern Marie Byrd Land, Antarctica. *Lithos*, 260, 134–153. <https://doi.org/10.1016/j.lithos.2016.05.018>
- Lloyd, A. J., Nyblade, A. A., Wiens, D. A., Hansen, S. E., Kanao, M., Shore, P. J., & Zhao, D. (2013). Upper mantle seismic structure beneath central East Antarctica from body wave tomography: Implications for the origin of the Gamburtsev Subglacial Mountains. *Geochemistry, Geophysics, Geosystems*, 14, 902–920. <https://doi.org/10.1002/ggge.20098>
- Lloyd, A. J., Wiens, D. A., Nyblade, A. A., Anandakrishnan, S., Aster, R. C., Huerta, A. D., et al. (2015). A seismic transect across West Antarctica: Evidence for mantle thermal anomalies beneath the Bentley Subglacial Trench and the Marie Byrd Land Dome. *Journal of Geophysical Research: Solid Earth*, 120, 8439–8460. <https://doi.org/10.1002/2015JB012455>
- Maaløe, S., & Aoki, K. (1977). The major element composition of the upper mantle estimated from the composition of lherzolites. *Contributions to Mineralogy and Petrology*, 63(2), 161–173. <https://doi.org/10.1007/BF00398777>
- Martinec, Z. (2014). Mass-density Green's functions for the gravitational gradient tensor at different heights. *Geophysical Journal International*, 196(3), 1455–1465. <https://doi.org/10.1093/gji/gjt495>
- Martin-Español, A., Bamber, J. L., & Zammit-Mangion, A. (2017). Constraining the mass balance of East Antarctica. *Geophysical Research Letters*, 44, 4168–4175. <https://doi.org/10.1002/2017GL072937>
- McDonough, W. F., & Sun, S.-S. (1995). The composition of the Earth. *Chemical Geology*, 120(3), 223–253.
- McKenzie, D., Jackson, J., & Priestley, K. (2005). Thermal structure of oceanic and continental lithosphere. *Earth and Planetary Science Letters*, 233(3–4), 337–349. <https://doi.org/10.1016/j.epsl.2005.02.005>
- Ménot, R.-P., Duclaux, G., Peucat, J. J., Rolland, Y., Guillot, S., Fanning, M., et al. (2007). Geology of the Terre Adélie Craton (135–146°E). In C. R. Raymond & A. K. Cooper (Eds.), *10th International Symposium on Antarctic Earth Sciences* (p. 1047). Santa Barbara, US: U.S. Geological Survey and The National Academies. <https://doi.org/10.3133/of2007-1047.srp048>
- Mitrovica, J. X., Gomez, N., Morrow, E., Hay, C., Latychev, K., & Tamisiea, M. E. (2011). On the robustness of predictions of sea level fingerprints. *Geophysical Journal International*, 187(2), 729–742. <https://doi.org/10.1111/j.1365-246X.2011.05090.x>
- Miyamachi, H., Toda, S., Matsushima, T., Takada, M., Watanabe, A., Yamashita, M., & Kanao, M. (2003). Seismic refraction and wide-angle reflection exploration by JARE-43 on Mizuho Plateau, East Antarctica. *Polar Geoscience*, 16, 1–21.
- Nield, G. A., Barletta, V. R., Bordoni, A., King, M. A., Whitehouse, P. L., Clarke, P. J., et al. (2014). Rapid bedrock uplift in the Antarctic Peninsula explained by viscoelastic response to recent ice unloading. *Earth and Planetary Science Letters*, 397, 32–41. <https://doi.org/10.1016/j.epsl.2014.04.019>
- Nield, G. A., Whitehouse, P. L., van der Wal, W., Blank, B., O'Donnell, J. P., & Stuart, G. W. (2018). The impact of lateral variations in lithospheric thickness on glacial isostatic adjustment in West Antarctica. *Geophysical Journal International*, 214(2), 811–824. <https://doi.org/10.1093/gji/ggy158>
- O'Donnell, J. P., & Nyblade, A. A. (2014). Antarctica's hypsometry and crustal thickness: Implications for the origin of anomalous topography in East Antarctica. *Earth and Planetary Science Letters*, 388, 143–155. <https://doi.org/10.1016/j.epsl.2013.11.051>
- O'Donnell, J. P., Selway, K., Nyblade, A. A., Brazier, R. A., Wiens, D. A., Anandakrishnan, S., et al. (2017). The uppermost mantle seismic velocity and viscosity structure of central West Antarctica. *Earth and Planetary Science Letters*, 472, 38–49. <https://doi.org/10.1016/j.epsl.2017.05.016>
- Pappa, F., Ebbing, J., & Ferraccioli, F. (2019). Moho depths of Antarctica: Comparison of seismic, gravity, and isostatic results. *Geochemistry, Geophysics, Geosystems*, 20(3), 1629–1645. <https://doi.org/10.1029/2018GC008111>
- Paulson, A., Zhong, S., & Wahr, J. (2005). Modelling post-glacial rebound with lateral viscosity variations. *Geophysical Journal International*, 163(1), 357–371. <https://doi.org/10.1111/j.1365-246X.2005.02645.x>
- Paxman, G. J. G., Watts, A. B., Ferraccioli, F., Jordan, T. A., Bell, R. E., Jamieson, S. S. R., & Finn, C. A. (2016). Erosion-driven uplift in the Gamburtsev Subglacial Mountains of East Antarctica. *Earth and Planetary Science Letters*, 452, 1–14. <https://doi.org/10.1016/j.epsl.2016.07.040>
- Paxman, G. J. G., Jamieson, S. S. R., Ferraccioli, F., Bentley, M. J., Ross, N., Watts, A. B., et al. (2019). The role of lithospheric flexure in the landscape evolution of the Wilkes Subglacial Basin and Transantarctic Mountains, East Antarctica. *Journal of Geophysical Research: Earth Surface*, 124, 812–829. <https://doi.org/10.1029/2018JF004705>
- Peltier, W. R. (2004). Global glacial isostasy and the surface of the ice-age Earth: The ICE-5G (VM2) Model and GRACE. *Annual Review of Earth and Planetary Sciences*, 32(1), 111–149. <https://doi.org/10.1146/annurev.earth.32.082503.144359>
- Peslier, A. H., Woodland, A. B., Bell, D. R., & Lazarov, M. (2010). Olivine water contents in the continental lithosphere and the longevity of cratons. *Nature*, 467, 78.
- Ramirez, C., Nyblade, A., Emry, E., Julià, J., Sun, X., Anandakrishnan, S., et al. (2017). Crustal structure of the Transantarctic Mountains, Ellsworth Mountains and Marie Byrd Land, Antarctica: Constraints on shear wave velocities, Poisson's ratios and Moho depths. *Geophysical Journal International*, 211(3), 1328–1340. Retrieved from <https://doi.org/10.1093/gji/ggx333>
- Ramirez, C., Nyblade, A., Hansen, S. E., Wiens, D. A., Anandakrishnan, S., Aster, R. C., et al. (2016). Crustal and upper-mantle structure beneath ice-covered regions in Antarctica from S-wave receiver functions and implications for heat flow. *Geophysical Journal International*, 204(3), 1636–1648. <https://doi.org/10.1093/gji/ggv542>
- Reading, A. M. (2006). The seismic structure of Precambrian and early Palaeozoic terranes in the Lambert Glacier region, East Antarctica. *Earth and Planetary Science Letters*, 244(1), 44–57. <https://doi.org/10.1016/j.epsl.2006.01.031>
- Riedel, S., Jacobs, J., & Jokat, W. (2013). Interpretation of new regional aeromagnetic data over Dronning Maud Land (East Antarctica). *Tectonophysics*, 585, 161–171. <https://doi.org/10.1016/j.tecto.2012.10.011>

- Riedel, S., Jokat, W., & Steinhage, D. (2012). Mapping tectonic provinces with airborne gravity and radar data in Dronning Maud Land, East Antarctica. *Geophysical Journal International*, 189(1), 414–427. <https://doi.org/10.1111/j.1365-246X.2012.05363.x>
- Ritzwoller, M. H., Shapiro, N. M., Levshin, A. L., & Leahy, G. M. (2001). Crustal and upper mantle structure beneath Antarctica and surrounding oceans. *Journal of Geophysical Research*, 106(B12), 30,645–30,670. <https://doi.org/10.1029/2001JB000179>
- Rose, K. C., Ferraccioli, F., Jamieson, S. S. R., Bell, R. E., Corr, H., Creyts, T. T., et al. (2013). Early East Antarctic Ice Sheet growth recorded in the landscape of the Gamburtsev Subglacial Mountains. *Earth and Planetary Science Letters*, 375, 1–12. <https://doi.org/10.1016/j.epsl.2013.03.053>
- Sato, H., & Sacks, I. S. (1989). Anelasticity and thermal structure of the oceanic upper mantle: Temperature calibration with heat flow data. *Journal of Geophysical Research*, 94(B5), 5705–5715. <https://doi.org/10.1029/JB094iB05p05705>
- Sato, H., Sacks, I. S., & Murase, T. (1989). The use of laboratory velocity data for estimating temperature and partial melt fraction in the low-velocity zone: Comparison with heat flow and electrical conductivity studies. *Journal of Geophysical Research*, 94(B5), 5689–5704. <https://doi.org/10.1029/JB094iB05p05689>
- Schaeffer, A. J., & Lebedev, S. (2013). Global shear speed structure of the upper mantle and transition zone. *Geophysical Journal International*, 194(1), 417–449. <https://doi.org/10.1093/gji/ggt095>
- Sclater, J. G., & Christie, P. A. F. (1980). Continental stretching: An explanation of the Post-Mid-Cretaceous subsidence of the central North Sea Basin. *Journal of Geophysical Research*, 85(B7), 3711–3739. <https://doi.org/10.1029/JB085iB07p03711>
- Seroussi, H., Ivins, E. R., Wiens, D. A., & Bondzio, J. (2017). Influence of a West Antarctic mantle plume on ice sheet basal conditions. *Journal of Geophysical Research: Solid Earth*, 122, 7127–7155. <https://doi.org/10.1002/2017JB014423>
- Shen, W., Wiens, D. A., Anandakrishnan, S., Aster, R. C., Gerstoft, P., Bromirski, P. D., et al. (2018). The crust and upper mantle structure of Central and West Antarctica from Bayesian inversion of Rayleigh wave and receiver functions. *Journal of Geophysical Research: Solid Earth*, 123, 7824–7849. <https://doi.org/10.1029/2017JB015346>
- Sigmundsson, F. (1991). Post-glacial rebound and asthenosphere viscosity in Iceland. *Geophysical Research Letters*, 18(6), 1131–1134. <https://doi.org/10.1029/91GL01342>
- Stixrude, L., & Lithgow-Bertelloni, C. (2005). Mineralogy and elasticity of the oceanic upper mantle: Origin of the low-velocity zone. *Journal of Geophysical Research*, 110, B03204. <https://doi.org/10.1029/2004JB002965>
- Storti, F., Balestrieri, M. L., Balsamo, F., & Rossetti, F. (2008). Structural and thermochronological constraints to the evolution of the West Antarctic Rift System in central Victoria Land. *Tectonics*, 27, TC4012. <https://doi.org/10.1029/2006TC002066>
- Thomas, I. D., King, M. A., Bentley, M. J., Whitehouse, P. L., Penna, N. T., Williams, S. D. P., et al. (2011). Widespread low rates of Antarctic glacial isostatic adjustment revealed by GPS observations. *Geophysical Research Letters*, 38, L22302. <https://doi.org/10.1029/2011GL049277>
- Torsvik, T. H., & Cocks, L. R. M. (2013). Gondwana from top to base in space and time. *Gondwana Research*, 24(3–4), 999–1030. <https://doi.org/10.1016/j.gr.2013.06.012>
- Uieda, L., Bomfim, E. P., Braatenberg, C., & Molina, E. (2011). Optimal forward calculation method of the Marussi tensor due to a geologic structure at GOCE height. *4th International GOCE User Workshop*, 696, 34.
- van der Wal, W., Barnhoorn, A., Stocchi, P., Gradmann, S., Wu, P., Drury, M., & Vermeersen, B. (2013). Glacial isostatic adjustment model with composite 3-D Earth rheology for Fennoscandia. *Geophysical Journal International*, 194(1), 61–77. <https://doi.org/10.1093/gji/ggt099>
- van der Wal, W., Whitehouse, P. L., & Schrama, E. J. O. (2015). Effect of {GIA} models with 3D composite mantle viscosity on {GRACE} mass balance estimates for Antarctica. *Earth and Planetary Science Letters*, 414, 134–143. <https://doi.org/10.1016/j.epsl.2015.01.001>
- van der Wal, W., Wu, P., Wang, H., & Sideris, M. G. (2010). Sea levels and uplift rate from composite rheology in glacial isostatic adjustment modeling. *Journal of Geodynamics*, 50(1), 38–48. <https://doi.org/10.1016/j.jog.2010.01.006>
- Vermeersen, L. A., & Sabadini, R. (1997). A new class of stratified viscoelastic models by analytical techniques. *Geophysical Journal International*, 129(3), 531–570. <https://doi.org/10.1111/j.1365-246X.1997.tb04492.x>
- von Frese, R. R. B., Potts, L. V., Wells, S. B., Leftwich, T. E., Kim, H. R., Kim, J. W., et al. (2009). GRACE gravity evidence for an impact basin in Wilkes Land, Antarctica. *Geochemistry, Geophysics, Geosystems*, 10, Q02014. <https://doi.org/10.1029/2008GC002149>
- Wannamaker, P., Hill, G., Stodt, J., Maris, V., Ogawa, Y., Selway, K., et al. (2017). Uplift of the central transantarctic mountains. *Nature Communications*, 8(1), 1588. <https://doi.org/10.1038/s41467-017-01577-2>
- Wessel, P., Smith, W. H. F., Scharroo, R., Luis, J., & Wobbe, F. (2013). Generic Mapping Tools: Improved Version Released. *Eos, Transactions American Geophysical Union*, 94(45), 409–410. <https://doi.org/10.1002/2013EO450001>
- White-Gaynor, A. L., Nyblade, A. A., Aster, R. C., Wiens, D. A., Bromirski, P. D., Gerstoft, P., et al. (2019). Heterogeneous upper mantle structure beneath the Ross Sea Embayment and Marie Byrd Land, West Antarctica, revealed by P-wave tomography. *Earth and Planetary Science Letters*, 513, 40–50. <https://doi.org/10.1016/j.epsl.2019.02.013>
- Whitehouse, P. L., Bentley, M. J., Milne, G. A., King, M. A., & Thomas, I. D. (2012). A new glacial isostatic adjustment model for Antarctica: Calibrated and tested using observations of relative sea-level change and present-day uplift rates. *Geophysical Journal International*, 190(3), 1464–1482. <https://doi.org/10.1111/j.1365-246X.2012.05577.x>
- Whittaker, J. M., Goncharov, A., Williams, S. E., Müller, R. D., & Leitchenkov, G. (2013). Global sediment thickness data set updated for the Australian-Antarctic Southern Ocean. *Geochemistry, Geophysics, Geosystems*, 14, 3297–3305. <https://doi.org/10.1002/ggge.20181>
- Wobbe, F., Lindeque, A., & Gohl, K. (2014). Total sediment thickness grid of the Southern Pacific Ocean off West Antarctica, links to NetCDF files. Retrieved from <https://doi.pangaea.de/10.1594/PANGAEA.835589>
- Wörner, G. (1999). Lithospheric dynamics and mantle sources of alkaline magmatism of the Cenozoic West Antarctic Rift System. *Global and Planetary Change*, 23(1), 61–77. [https://doi.org/10.1016/S0921-8181\(99\)00051-X](https://doi.org/10.1016/S0921-8181(99)00051-X)
- Wu, P. (2004). Using commercial finite element packages for the study of earth deformations, sea levels and the state of stress. *Geophysical Journal International*, 158(2), 401–408. <https://doi.org/10.1111/j.1365-246X.2004.02338.x>
- Wu, P. (2005). Effects of lateral variations in lithospheric thickness and mantle viscosity on glacially induced surface motion in Laurentia. *Earth and Planetary Science Letters*, 235(3), 549–563. <https://doi.org/10.1016/j.epsl.2005.04.038>
- Yoshii, K., Ito, K., Miyamachi, H., & Kanao, M. (2004). Crustal structure derived from seismic refractions and wide-angle reflections in the Mizuho Plateau, East Antarctica. *Polar Geoscience*, 17, 112–138.